Electrical Impedance Tomography for Biomedical Applications: Circuits and Systems Review

YU WU [1] (Member, IEEE), **FARNAZ FAHIMI HANZAEE** [1] (Student Member, IEEE),
DAI JIANG [1] (Senior Member, IEEE), **RICHARD H. BAYFORD** [2] (Life Senior Member, IEEE),
AND ANDREAS DEMOSTHENOUS [1] (Fellow, IEEE)

(Invited Paper)

[1] Department of Electronic and Electrical Engineering, University College London, London WC1E 7JE, U.K.

[2] Department of Natural Sciences, Middlesex University, London NW4 4BT, U.K.

This article was recommended by Associate Editor A. Burdett.

CORRESPONDING AUTHOR: A. DEMOSTHENOUS (e-mail: a.demosthenous@ucl.ac.uk)

ABSTRACT There has been considerable interest in electrical impedance tomography (EIT) to provide low-cost, radiation-free, real-time and wearable means for physiological status monitoring. To be competitive with other well-established imaging modalities, it is important to understand the requirements of the specific application and determine a suitable system design. This paper presents an overview of EIT circuits and systems including architectures, current drivers, analog front-end and demodulation circuits, with emphasis on integrated circuit implementations. Commonly used circuit topologies are detailed, and tradeoffs are discussed to aid in choosing an appropriate design based on the application and system priorities. The paper also describes a number of integrated EIT systems for biomedical applications, as well as discussing current challenges and possible future directions.

INDEX TERMS Analog front-end, bioimpedance, current driver, demodulation, electrical impedance tomography (EIT), integrated circuits, wearable technologies.

I. INTRODUCTION

SINCE the first commercial and clinical electrical impedance tomography (EIT) system was developed by Barber and Brown in the mid-1980s [1], [2] many research groups have focused on improving the method and incorporating it in various biomedical applications [3]. Studying the electrical properties of the human body has revealed that different tissues exhibit distinct bioimpedance characteristics [4], [5]. These are in the form of a complex value where the real part is associated with the fluid and blood content of the organ, and the imaginary part is related to the capacitance effect of the biological cell's phospholipid membrane [6]–[8].

EIT is based on the bioimpedance measurement technique, which entails measuring the voltage developed on the test subject due to a known current injection and calculating its impedance. Depending on the application, the frequency of the injected current can be chosen to be a high range (up to 10 MHz) where the resultant impedance is mostly due to the liquid content of the tissue. On the other hand, injecting a current at a low frequency range (as low as a few Hz) results in an impedance that represents the shape and volume of the target tissue [7]. Some of the commonly used frequency ranges for each application are provided in Section II. Compared to other more established, non-invasive, imaging techniques such as magnetic resonance imaging (MRI) and X-ray computed tomography (CT), bioimpedance analysis has the advantages of being radiation-free (as is MRI), low-cost, portable, having the potential to be miniaturized and suitable for continuous and bedside real-time monitoring [9], [10]. Although EIT cannot currently compete with the high spatial resolution and accuracy of

MRI and CT, it has significant potential to be used in parallel to overcome many of their shortcomings [7].

This paper presents an overview of circuits and systems for biomedical EIT focusing on integrated implementations. A number of architectures, methods and circuits, and the latest integrated implementations are discussed, and insights are provided to demystify the design of EIT systems. The rest of the paper is organized as follows. Biomedical applications of EIT are elaborated in Section II. System architectures and demodulation methods are reviewed in Section III. Circuits for the analog front-end is the focus of Section IV. Recent integrated EIT systems are discussed in Section V. Section VI outlines challenges with the use of current EIT systems in a clinical environment as well as suggesting possible future directions. Concluding remarks are drawn in Section VII.

II. EIT IN BIOMEDICAL APPLICATIONS
A. LUNG VENTILATION MONITORING
While single channel bioimpedance recording could be used to detect basic respiration cycles [11], [12] in order to obtain more in-depth clinical information, real-time imaging of the respiratory status has been the most studied application of EIT. This provides a low-cost means for clinical monitoring of patients under critical care whose lung function has been affected by a pulmonary-related disease and/or congenital conditions [4], [13], [14]. Notable contrast can be detected between the lung resistance and the normal thorax tissue due to the higher resistivity of the air content of the lungs [15], [16]. Regional or global variation in the tissue impedance can be monitored by measuring the voltage resulting from the injection of a current, commonly around 50 kHz. The impedance distribution can represent changes in the volume of gas (air) and fluid (blood) during the respiratory cycle and under various pathological conditions [3], [16]. Variables including cardiac activity and tissue movement can adversely affect the accuracy of the measured impedance, and therefore the system must be carefully designed to reduce the effect of such unwanted signals [17].

The fact that EIT enables bedside monitoring and circumvents the need for patients to be sedated or exposed to radiation, makes it a viable imaging technique both for adult and pediatric patients [18]. It can help clinicians to ensure that lung collapse does not occur in patients under mechanical ventilation by patient-specific adjustment of the ventilator parameters such as tidal volume, rate and pressure [19], [20]. Furthermore, in preterm neonates, given the higher risk of respiratory distress, continuous monitoring of lung dynamics can prevent long-term morbidity [21]. Due to the significant variation in the lung electrical impedance characteristics between neonatal and adult patients (where higher resistivity and lower sensitivity to frequency changes are observed in neonates), EIT can be used in investigations of human lung development.

B. CARDIAC IMAGING
The application of EIT in monitoring patients with cardiovascular disease mainly originates from the distinctive difference in the resistivity of blood compared to the surrounding heart muscle, bone and fat tissue [2], [22]. Recording the thoracic impedance distribution at each cardiac cycle can provide valuable information regarding blood perfusion and consequently the stroke volume (SV; the volume of blood that is pumped by each ventricle during each heartbeat) and the cardiac output (SV × beat rate). Deficiencies including the blockage of coronary arteries by atherosclerotic plaques may impede the heart from properly playing its role in delivering oxygenated blood [23]. By routine monitoring of the variation of cardiac impedance, heart failure can conceivably be prevented in many cases.

Applying a mid-to-high frequency (10 Hz to 1 MHz) and low-amplitude current (< 1 mA) results in a measured cardiac-related bioimpedance which is relatively smaller than the impedance values recorded for lung ventilation EIT. This makes cardiac EIT more sensitive to noise [24]. Also, the variation in the resistivity of organs in the vicinity of the heart and the movement of the heart itself can limit the accuracy of this imaging technique and hinder the widespread clinical use of EIT systems for this application [25], [26]. This issue notwithstanding, the advantages offered by EIT can compensate for the disadvantages of conventional methods such as X-ray-based CT scans and angiography, or ultrasound-based echocardiography [23]. Effort is also being devoted to improving the performance of EIT systems to provide an alternative to bulky and/or invasive imaging modalities. This could pave the path toward a wearable device that enables early diagnosis of heart failure and even facilitate cardiac telemonitoring by patients and clinicians [22], [27], [28].

C. BRAIN ACTIVITY MONITORING
EIT has applications in neuroscience and regional as well as global brain imaging. Displacement of conductive fluid (i.e., blood and cerebrospinal fluid) and any variation in its flow or volume in the brain can lead to impedance changes that are detectable by measuring the boundary voltage induced by an alternating current of smaller than 1 mA and below 100 kHz [29]. Changes in blood flow are also the underlying basis of functional imaging techniques such as positron emission tomography (PET) (which is often combined with CT X-ray scans) and functional MRI (fMRI) that can provide high spatial resolution but with no prospect of bedside real-time monitoring [30], [31].

In this application, the presence of the high resistance skull bone tissue, with thickness values varying from patient to patient, can limit the impedance contrast due to the restricted amount of injectable current reaching the brain. Nevertheless, in conditions such as cerebral ischemia, a significant increase of 20-200% in impedance has been observed [32]. This variation in impedance is thought to be mainly because of the

increased flow of ion-containing and low-resistance extra-cellular fluid into brain cells, causing cellular swelling and tissue edema [33]. This appreciably increases the impedance of the extracellular space [31]. Consequently, monitoring this impedance variation can be used for early diagnosis of brain ischemia and stroke in patients with traumatic brain injury [34].

In neonates, the lower resistivity of skull bone tissue makes EIT a suitable candidate for imaging brain structural abnormalities [31], [32], [35]. More generally, EIT has also proved to be useful in other neurological applications in clinical situations such as localizing the seizure focus on epilepsy and detecting physiological stimulation responses.

D. CANCER DIAGNOSIS

For at least the past one hundred years, researchers have shown that the electrical properties of malignant cancerous tissue differ notably from those of healthy tissue [36]. Therefore, bioimpedance analysis can be a suitable candidate for the preliminary diagnosis of tumors in, for example, breast or prostate tissue. Early studies showed that cell swelling in tumor tissue causes an increase of conductivity due to a rise in the fluid content of cells which occurs following membrane disruption [37], [38]. Since the phospholipid membrane has a capacitive electrical property, the higher permittivity of cancerous cells can result in a higher capacitance in cancerous tissue [39].

In the case of prostate cancer, the current common diagnostic method is to use transrectal ultrasound (TRUS) imaging as guidance for biopsy to determine the stage of the cancer. However, the limited accuracy of this method raises the need for a more reliable screening technique [40], [41]. Researchers have developed an ultrasound-coupled transrectal EIT (TREIT) system, based on both ultrasound and impedance tomography, in order to enhance the quality of EIT image reconstruction and better localize the target area for biopsy [42]–[44]. To obtain a distinctive impedance contrast between cancerous and benign tissue, applying a current with a frequency higher than 100 kHz is recommended which makes the circuit design more challenging [43].

The current standard screening protocol for breast cancer is X-ray mammography. An analysis in 2011 revealed that within a 10-year screening window, 7-9% of patients receive a false-positive referral for biopsy follow-up [45] (see also [46]). It is possible that a sufficiently developed EIT system could complement the current screening protocols by providing a small and portable device, especially with the ability of three-dimensional (3D) imaging, which could open up new possibilities for home examination [47]–[49] and even aid with classification of tumor type [50].

E. EMERGING BIOMEDICAL APPLICATIONS

EIT has received significant attention in many other areas, for example, in tissue engineering to monitor cell growth [51], sport science and the assessment of post-exercise muscle changes [52], body composition

analysis [53], [54], monitoring nutritional status [55], and gastrointestinal function [56]. More recently, research on EIT has been applied to human-machine interface devices [57] and neural activity monitoring [58].

III. ARCHITECTURES AND DEMODULATION METHODS
A. GENERAL OVERVIEW

EIT systems are based on applying a small alternating current, with a specific frequency, between one pair of electrodes (e.g., placed in a ring-shaped configuration on the boundary of the test subject) and measuring the resultant voltage from the remaining pairs of electrodes at the surface [29]. Knowing the current and voltage values, the interior impedance of the tissue can be calculated and then a conductivity map reconstucted using a number of repeating measurements that form a tomography-like image [59].

Based on the above requirements, an EIT circuit consists of two main blocks: (i) the system front-end including a current driving circuit and a voltage readout, and (ii) the back-end for system operation control and impedance demodulation, as shown in Fig. 1(a). The front-end is directly coupled to the electrodes which are labeled E1 to E8 in Fig. 1(a). EIT uses various types of predefined measurement sequence, the most common being the 'adjacent-scan pattern' [60]. In this pattern, a current is sequentially injected between two adjacent electrodes during each scan cycle. The resulting voltage potentials are measured on all other adjacent electrode pairs as shown in Fig. 1(a). Once all the voltages are recorded in a scan cycle, the current injection moves to the next pair of electrodes and the cycle continues until all adjacent electrode pairs have been used for current injection with all corresponding voltages recorded. Thus, for n electrodes, there are $n \times n$ voltages measured in total (voltages that involve injecting electrodes are not used for imaging). This collection of voltages is called a 'frame of dataset' which can be used to generate one frame of image. For the adjacent-scan pattern, there is only one active current driver during each scan cycle; however, the voltages can be measured either sequentially or simultaneously. This concerns the design of electrode multiplexing circuits in the system front-end.

The system back-end has two main functions: (i) controlling the front-end according to the scan pattern, and (ii) receiving the voltage data and converting it to impedance information that can be used for imaging. This process is called *impedance demodulation*. The system back-end communicates with an imager, e.g., a personal computer. The imager uses an inverse-problem solver algorithm that translates the impedance data into an impedance distribution map (image) [61]. As shown in Fig. 1(b), the solver creates a finite element model (FEM) matching the contour shape of the test subject as the boundary condition. Using time-differencing, the solver reconstructs an image showing the impedance redistribution occurred Δt later in time compared to the initial state that is defined by a reference dataset frame. To better explain time-differencing, the test subject shown
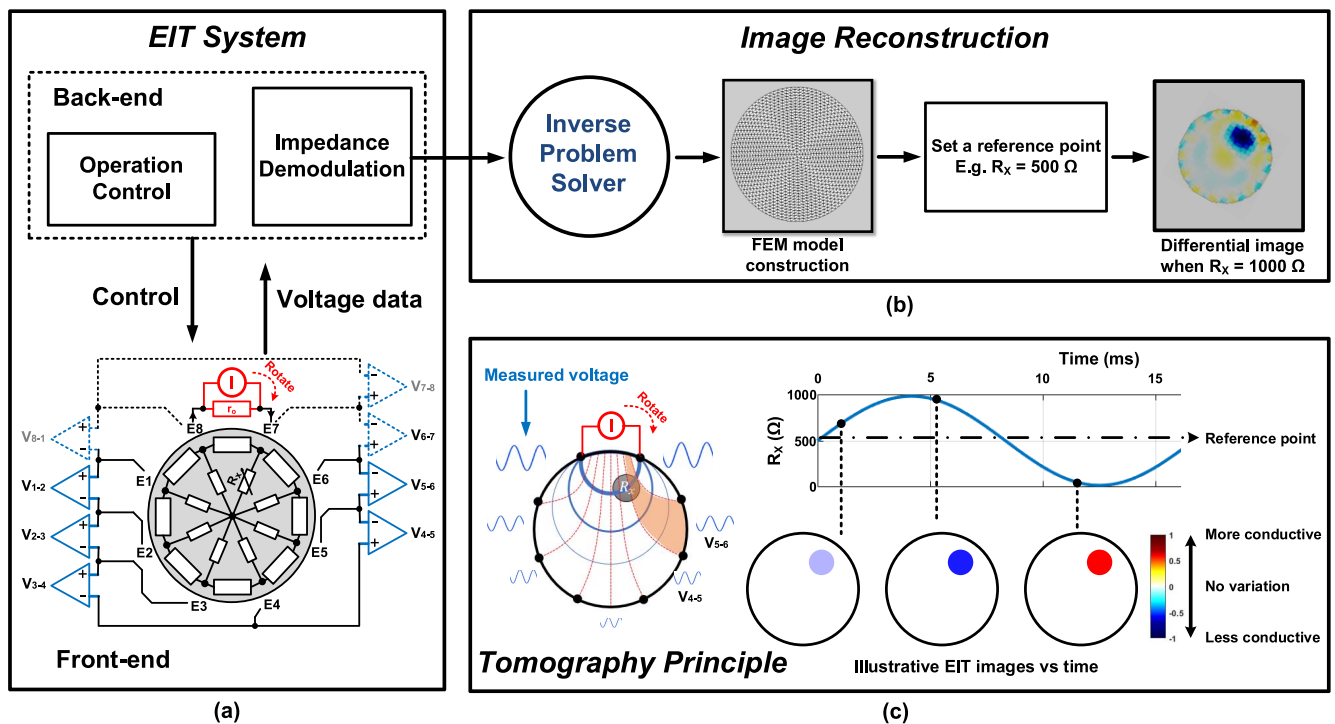
FIGURE 1. EIT system overview and operating principles. (a) EIT system and operation; (b) image reconstruction flow; and (c) tomography principle with demonstrative EIT images.

in Fig. 1(a) has been modeled by a resistive mesh network (a 'phantom') which simulates the internal bioimpedance structure of the test object. Such a phantom is commonly used for EIT system evaluation [62]. Inside the phantom, there is a variable element R_x. As shown in Fig. 1(b), the inverse-problem solver takes a reference dataset frame, e.g., when $R_x = 500$ Ω, then processes it together with another dataset frame, Δt later when $R_x = 1$ kΩ. The output image will then show the resultant conductivity redistribution. Any static element, for example, the voltage due to the sternum and rib cage while imaging the respiration of lungs, can be suppressed to better illustrate biological variations.

Fig. 1(c) shows the simplified tomography principle used to create the image. The blue lines indicate the injected current flow, and the red-dotted lines are the equipotentials. In the case of adjacent scans, the current density decreases at locations far from the injection site. This causes a unique voltage amplitude pattern often referred to as the 'U'-shaped pattern (the closer the electrodes are to the current injection site, the higher the voltage becomes). This characteristic defines the hardware implementation (discussed in Section IV). The developed voltage also reflects the impedance characteristic under the regions over which the electrode pair measures, e.g., V_{5-6} concerns the shaped region shown in Fig. 1(c). As R_x varies, the equivalent impedance of the shaped region, and consequently the amplitude of V_{5-6}, changes accordingly. An image can then be reconstructed with a collection of color-weighted regions

overlapping together. Fig. 1(c) also shows that as R_x varies in time, EIT can reconstruct the location in which the variation occurs and determine the level of its impedance variation through color-mapping.

As noted for different applications in Section II, the frequency of the applied current also reflects the impedance characteristics of tissues. Therefore, in addition to the time-differencing imaging technique, frequency-differencing is an equally important technique used in EIT. In this method, instead of having two datasets taken with a time delay to reflect temporal changes, two frequencies are measured to produce an image that could reflect absolute tissue properties.

EIT imaging can offer high temporal resolution, while the spatial image resolution is determined by the number of electrodes used. When high electrode counts are adopted, the EIT system must scan all the electrodes and conduct tomography computation faster to maintain the same level of temporal resolution. Solving the inverse-problem for the tomography image is an important and challenging task. The algorithms attempt to solve a mathematically ill-posed problem, and a small amount of noise within the measured data can result in large errors [63]. Among many challenges, one that most concerns the hardware is due to the finite number of electrodes; the number of measured data is often fewer than that of the conductivity elements in the FEM. In addition, the voltages associated with the injecting electrodes must be excluded in the image reconstruction (for a detailed
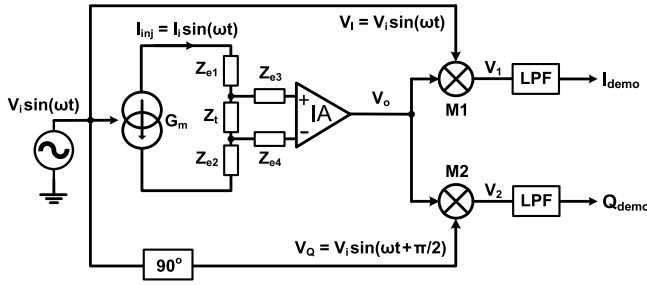
FIGURE 2. I-Q demodulation with tetrapolar electrodes. G_m is the transconductance of the current driver, $Z_{e1,2,3,4}$, are the electrode impedances, Z_t is the tissue impedance, M1 and M2 are multipliers, and LPF are low-pass filters.

explanation, see Section IV). Due to the nature of solving an ill-posed inverse problem during image reconstruction, EIT images do not offer high spatial resolution, and this poses a continuing challenge. Another practical limitation is that the image reconstruction algorithm is based on a static FEM that considers all electrodes to be evenly distributed around the subject. Displacement of the electrodes and physical shape deformation of the subject can all contribute to image artifacts [64]–[66]. This review paper mainly focuses on the hardware design and implementation of the parts of the EIT system before the imager.

B. IMPEDANCE DEMODULATION

Impedance demodulation is the process of extracting the amplitude and phase delay of the measured voltage which can then be used for bioimpedance mapping. The relationship between impedance (Z), amplitude (A) and phase delay (θ) can be written as $Z = R + jX = Ae^{j\theta}$.

1) I-Q DEMODULATION

One of the most frequently used demodulation methods in bioimpedance monitoring is in-phase and quadrature-phase (I-Q) demodulation (also known as coherent demodulation or synchronous detection) which uses a single tone sinewave. As shown in Fig. 2, an input sinusoidal voltage signal, $V_i\sin(\omega t)$ (where V_i is the voltage amplitude, and $\omega = 2\pi f$), drives a current source of transconductance G_m, generating current $I_{inj} = G_m V_i\sin(\omega t) = I_i\sin(\omega t)$ that is injected into the tissue. The current is injected through a pair of electrodes $(Z_{e1,2})$ and the resulting surface voltage is recorded through another pair of electrodes $(Z_{e3,4})$. The voltage measured at the output of the front-end instrumentation amplifier (IA) is given by:

$$V_o = A_v Z_t I_i\sin(\omega t - \theta) \qquad (1)$$

where A_v is the gain of the IA, Z_t is the tissue impedance and θ is a phase delay relative to I_{inj}. The input voltage signal is used to generate two demodulation signals: one which is in-phase with the injected signal [$V_I = V_i\sin(\omega t)$] and another which is phase shifted by 90 degrees [$V_Q = V_i\sin(\omega t + \frac{\pi}{2})$]; both are multiplied with the measured output voltage V_o.

For the in-phase channel:

$$V_1 = V_o \times V_I = A_v Z_t I_i\sin(\omega t - \theta) \times V_i\sin(\omega t)$$
$$= \frac{A_v Z_t I_i V_i}{2}[\cos(\theta) - \cos(2\omega t - \theta)]. \quad (2)$$

For the quadrature-phase channel:

$$V_2 = V_o \times V_Q = A_v Z_t I_i\sin(\omega t - \theta) \times V_i\sin\left(\omega t + \frac{\pi}{2}\right)$$
$$= \frac{A_v Z_t I_i V_i}{2}\left[\cos\left(\theta + \frac{\pi}{2}\right) - \cos\left(2\omega t - \theta + \frac{\pi}{2}\right)\right].$$
$$(3)$$

The output of each multiplier (M1 and M2) is subsequently low-pass filtered to remove the double frequency components, resulting in two dc components:

$$I_{demo} = \frac{A_v Z_t I_i V_i}{2}\cos(\theta) \qquad (4)$$

and

$$Q_{demo} = \frac{A_v Z_t I_i V_i}{2}\sin(\theta). \qquad (5)$$

Dividing the above equations by the factor $(A_v I_i V_i)/2$, the amplitude and phase of V_o (and hence the real and imaginary components of the tissue impedance Z_t) can be obtained.

The I-Q demodulation can be performed with either analog or digital demodulation. With analog implementation, the in-phase and quadrature-phase signals can be generated by, for example, a quadrature oscillator. After the I-Q signals are multiplied by the measured voltage, the result is low-pass filtered in the analog domain and the final dc signals are then digitized. For digital implementation, a digital-to-analog converter (DAC)-based direct digital synthesizer (DDS) can be used for signal generation. An analog-to-digital converter (ADC) converts the output of the front-end IA (V_o) directly to the digital domain. Using the pre-stored I and Q signals from the DDS together with, for example, two multiplier-accumulator (MAC) units, the digitized V_o can be demodulated.

Digital signal processing, for example with a field-programmable gate array (FPGA), offers high-speed, precise and flexible control at the expense of a higher power consumption. For analog processing, the challenge lies in producing precise wideband I-Q signals, and high-performance analog multipliers. A comparison study was performed in [67] to obtain a matched noise performance, and a processing time of 300 μs for a 10 kHz excitation signal with a noise level of 1 mV$_{rms}$. The results revealed that the analog approach requires an eighth-order low-pass filter for an acceptable settling time and a 14-bit, 2.1 mega samples per second (MSPS) ADC. The ADC samples are averaged to improve the signal-to-noise ratio (SNR) and the noted sample rate is set to capture enough samples from the dc signal within one period of the recorded signal. In contrast, the digital approach only requires a 10-bit, 0.88 MSPS ADC for 300 μs processing time. Overall, the choice between analog or digital I-Q demodulation is a tradeoff between SNR, power consumption, and the required image frames per second (fps) for the target application.

2) ADVANCES IN I-Q DEMODULATION

In more recent designs, particularly for CMOS integrated EITs where the circuit design can be highly specialized, mixed-signal demodulation is a more popular approach. An alternative to the conventional single-tone sinusoid I-Q system uses square waveforms for demodulation. The common practice is to demodulate (i) sine, (ii) square or (iii) pseudo-sine signal excitation using square waves [68]–[70].

Scenario I (Sine Excitation and Square Demodulation): The Fourier series of a square waveform is expressed as:

$$V_{i\_square} = \frac{4}{\pi} \sum_{n=1,3,5...}^{\infty} \frac{\sin(n\omega t)}{n} \qquad (6)$$

where ω is the fundamental frequency of the square and sine wave signals, and n is the harmonic number. Considering the in-phase channel with a square wave signal, multiplication of the output signal from (1) with the square wave yields:

$$V_{i\_square} \times V_o = \frac{2A_v Z_t I_i}{\pi}[\cos(\theta) - \cos(2\omega t - \theta)] \qquad (7)$$

with the added harmonics:

$$\frac{2A_v Z_t I_i}{\pi} \left\{ \frac{\cos(2\omega t + \theta) - \cos(4\omega t - \theta)}{3} + \cdots \right.$$
$$\left. + \frac{\cos((n-1)\omega t + \theta) - \cos((n+1)\omega t - \theta)}{n} \right\}. \quad (8)$$

After low-pass filtering the desired dc components are obtained.

This approach is favored for CMOS implementations as the multiplier can be merged into the analog front-end in the form of chopper switches [68], [71] and the DDS method is often used for generating the input voltage signal (or the injecting current I_{inj}) as previously mentioned. To achieve better power efficiency, a tradeoff exists between using single-tone, pseudo-sine or square waves and measurement accuracy. This mainly concerns the harmonic dc fold-back error.

Scenario II (Square Excitation and Square Demodulation): A simpler and more power efficient system uses square wave injection with chopper demodulation. The final dc value after low-pass filtering in the case of in-phase demodulation is expressed as:

$$I_{demo} = \frac{8}{\pi^2} \sum_{n=1,3,5...}^{\infty} \frac{A_v Z_t I_i V_i(n\omega)\cos[\theta(n\omega)]}{n^2} \qquad (9)$$

where $A_v Z_t I_i V_i(n\omega)$ is the amplitude and $\theta(n\omega)$ is the phase of V_o at the fundamental and n^{th} harmonic and the other variables are as previously defined. In (9) the desired demodulated dc output is obtained only when $n = 1$ and the rest ($n > 1$) are fold-back errors. A technique for dc error cancellation is described in [72], where an algorithm interpolates the magnitude of harmonic frequencies for error cancelation at the expense of extra processing power.
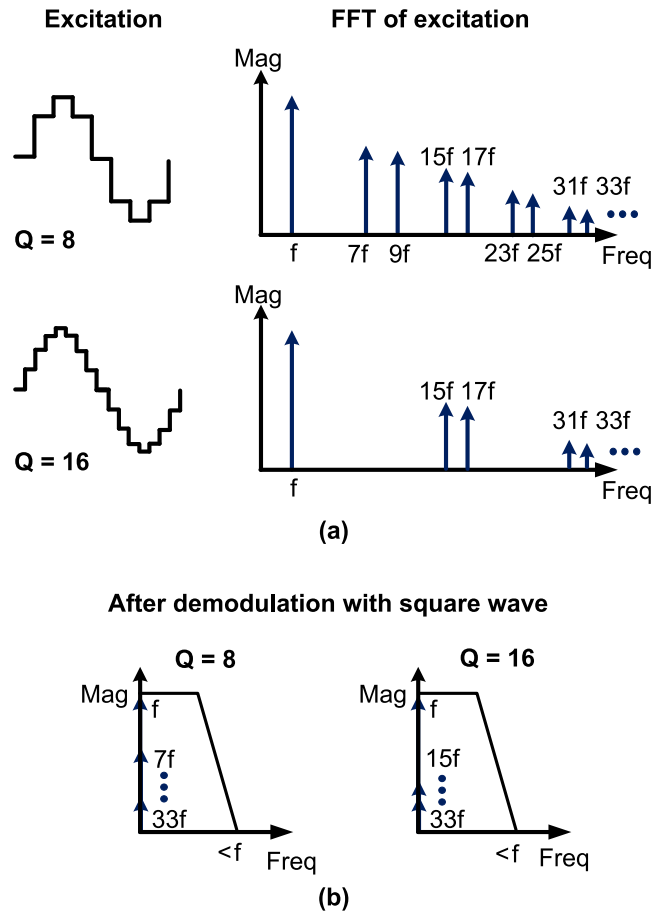
FIGURE 3. (a) Excitation with pseudo-sine wave using 8 and 16 quantization levels and the corresponding FFT according to Eq. (10). (b) The demodulated dc output through a square wave and a low-pass filter with a cut-off frequency of less than the fundamental frequency. Note that the magnitude of each frequency component is not to scale. *Q* is the quantization level and *f* is the fundamental frequency.

Scenario III (Pseudo-Sine Excitation and Square Demodulation): The performance of pseudo-sine excitation depends on the number of quantization levels (i.e., the total number of samples used in every pseudo-sine cycle). A pseudo-sine signal generated using DDS has harmonics in pairs and the frequencies of the harmonic pairs can be expressed as:

$$\omega_{harm}(N \pm 1) = (QN \pm 1)\omega_{fund}; \quad N = 1, 2, 3 \dots \quad (10)$$

where ω_{harm} is the harmonic frequency and ω_{fund} is the fundamental frequency, Q is the quantization level and N is the order of the harmonic pairs. The amplitude coefficient of the pseudo-sine fundamental frequency is:

$$C_{fund} = \frac{1}{2}\left|\text{sinc}\left\{\frac{\pi}{Q}\right\}\right|. \qquad (11)$$

The amplitude coefficient of the harmonic pair C_{harm} can be approximated as:

$$C_{harm(N\pm1)} = \frac{1}{2}\left|\frac{\text{sinc}\left\{\frac{\pi}{QN}\right\}}{QN \pm 1}\right|; N = 1, 2, 3 \cdots \qquad (12)$$

For detailed analysis see [73].

As an example, two excitation pseudo-sine wave signals using $Q = 8$ and $Q = 16$ are shown in Fig. 3 together with plots of their frequency spectra. The frequency components of the harmonic pairs are identified according to (10), e.g., for $Q = 8$, the first-order harmonic pair is located at $7f_{fund}$ and $9f_{fund}$. The magnitude of each component can be derived from (11) and (12). The higher harmonic components result in smaller dc fold-back errors due to the lower amplitude coefficients both for the pseudo-sine and square waves. With additional levels of quantization, lower harmonics can be removed to achieve better accuracy at the expense of circuit design complexity.

Fig. 4(a) shows the theoretical percentage accuracy for the in-phase component when using different quantization levels. The demodulator uses a square wave with an ideal low-pass filter having a cut-off at the fundamental frequency. The graphs indicate an accuracy of around 95% for 8 levels of quantization. After demodulation, the largest harmonic component is located at the $2f_{fund}$ frequency which needs to be rejected. Fig. 4(b) shows the ratio between the dc and the $2f_{fund}$ frequency components for different quantization levels. This ratio should be taken into account in the design of the low-pass filter, including the cut-off frequency, number of orders and settling time. In terms of design considerations, these different I-Q demodulation methods are a tradeoff between hardware complexity and measurement accuracy. For point-of-care applications, Scenario III could offer the best solution. In contrast, for a standalone medical device as used in an intensive care unit, conventional I-Q (described in Section III.B.1) could be considered to offer the best accuracy.

3) MAGNITUDE AND PHASE DETECTION

Using magnitude and phase demodulation, the amplitude and phase delay of the output signal (A and θ shown in Fig. 5(a)) can be directly measured. The principle behind the phase detector shown in Fig. 5(b) is that the two comparators check for the zero-crossing points of the measured (V_m) and reference (V_r) signals (V_r can be the in-phase signal mentioned in Section III.B.1), and through an XOR gate the time elapsed between the two zero-crossing points is registered by a counter for phase delay extraction.

As for the magnitude detection, Fig. 5(b) shows the simplest implementation for peak detection comprising a diode and a capacitor. A more detailed circuit would include an opamp that compensates for the diode voltage drop, as is commonly seen in discrete implementations.

In CMOS design, a common practice is to use an opamp with a negative feedback configuration to drive a PMOS transistor charging a capacitor (Fig. 6(a)) or a comparator driving a switch that opens when the peak value of the input has been sampled to a capacitor (Fig. 6(b)). A more advanced implementation is shown in Fig. 6(c) that uses the comparator output as a latched signal. While the comparator output is high, a capacitor is periodically charged by a current mirror. The comparator output becomes low once the input peak
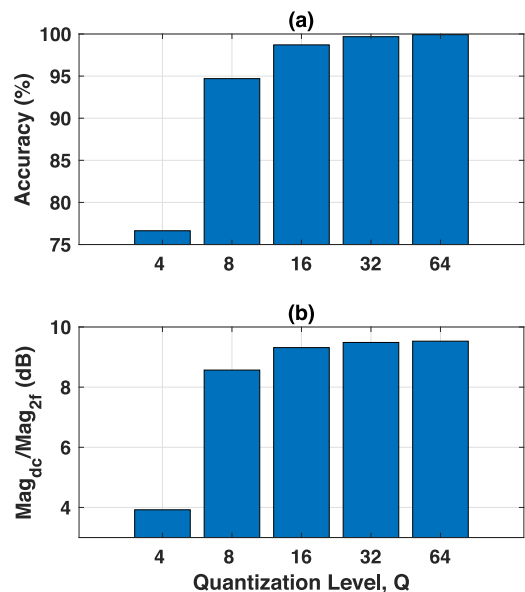

FIGURE 4. (a) Percentage accuracy versus quantization level. (b) Difference between the magnitude of the dc component and the $2f_{fund}$ frequency component.
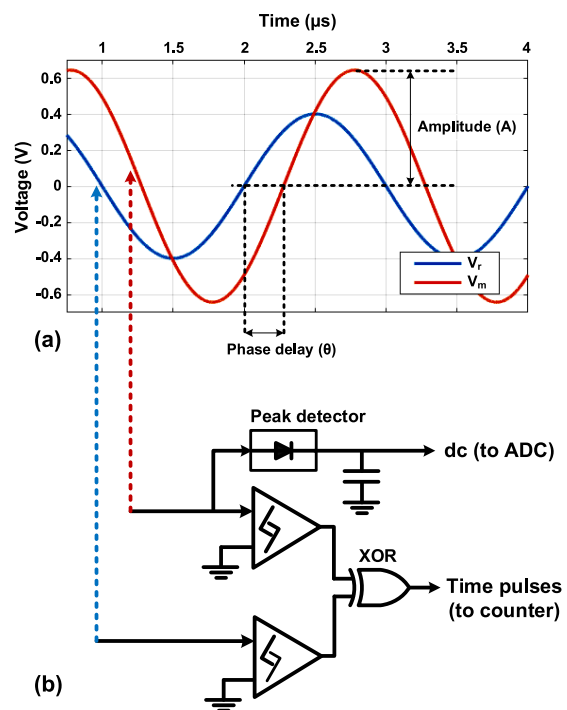

FIGURE 5. (a) The principle of the magnitude and phase demodulation method, and (b) its circuit implementation.

value is reached and a counter registers the total number of charging periods. The merit of the magnitude and phase detection method is its simplicity, but challenges may lie in dealing with noise and dc offsets.

4) OTHER DEMODULATION METHODS

Other demodulation methods reported in the literature utilize a direct time-to-digital approach. It offers low power and
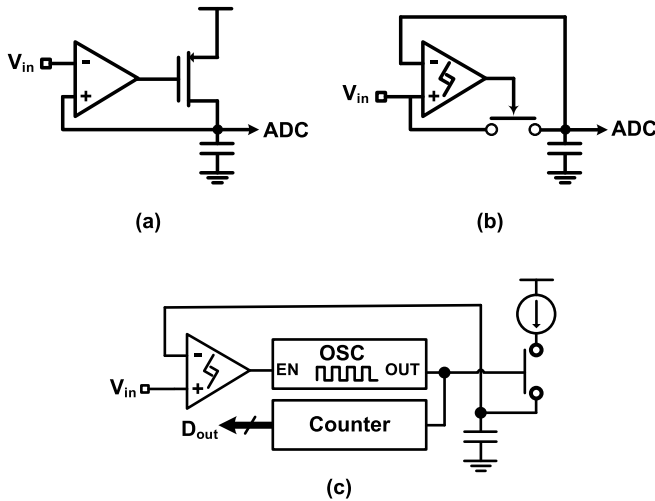
FIGURE 6. Capacitor charging peak detector. (a) Opamp-based, (b) comparator-based, and (c) comparator hybrid with digital conversion.
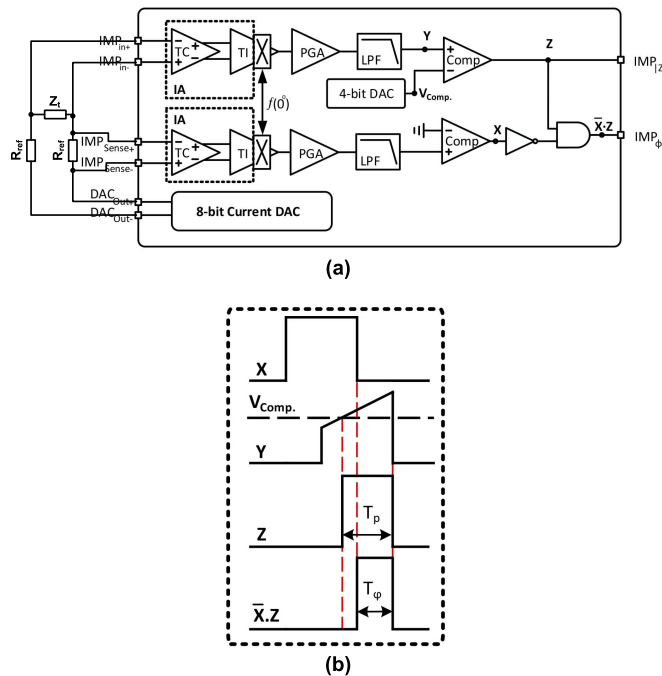

FIGURE 7. The principle of the pulse-width modulation method [74]. (a) System diagram and (b) signals at different nodes of the amplitude and phase channels.

direct digitization with less complex circuits. Below, two implementations of this approach are discussed.

1) Pulse-Width Demodulation: This method uses a unique semi-ramp signal as the current output [74]. The DAC differential output current is injected to the bio-sample Z_t through resistors R_{ref}. This arrangement provides a reference signal (IMP_{sense}) and the input signal (IMP_{in}) which are measured by the two recording channels in Fig. 7(a). The measured signals are then modulated by the fundamental frequency $f_{(0°)}$ using the chopping technique. After chopping, the semi-ramp signal only has the positive half shown as signal Y in Fig. 7(b). This signal is then compared with a voltage V_{comp}.
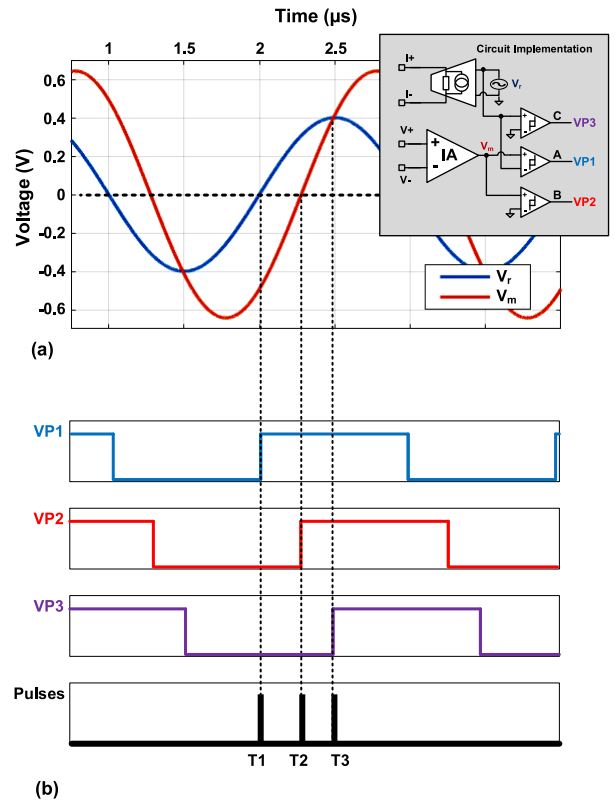

FIGURE 8. The principle of the time stamp demodulation method [75]. Signals (a) before demodulation and (b) after demodulation.

generated by a DAC which results in signal Z (IMP_Z). In the IMP_{sense} branch, signal X represents the zero-crossing of the differential input signal IMP_{in}, and an AND operation between the inverted X and Z results in IMP_ϕ. The magnitude and phase information of the bio-sample are then embedded in the pulse-width of the outputs IMP_Z and IMP_ϕ.

2) Time Stamp Demodulation: The time stamp method [75] uses only three comparators for demodulation as shown in Fig. 8(a). For phase detection, comparator A identifies the zero-crossing of the reference sine signal V_r at time $T1$ and comparator B identifies the zero-crossing of the measured sine signal V_m at time $T2$. Using the time stamps $T1$ and $T2$, the phase can be measured.

To measure the amplitude of V_m, comparator C identifies the crossing points between V_r and V_m which provides time stamp $T3$. As the amplitude of the reference signal V_r is known, the voltage amplitude at $T3$ can be obtained from:

$$V_{T3} = V_r \sin[2\pi f(T3 - T1)]. \tag{13}$$

The unknown amplitude A_{Vm} of the measured signal V_m can then be derived:

$$A_{Vm} = \frac{V_{T3}}{\sin[2\pi f(T3 - T2)]}. \tag{14}$$

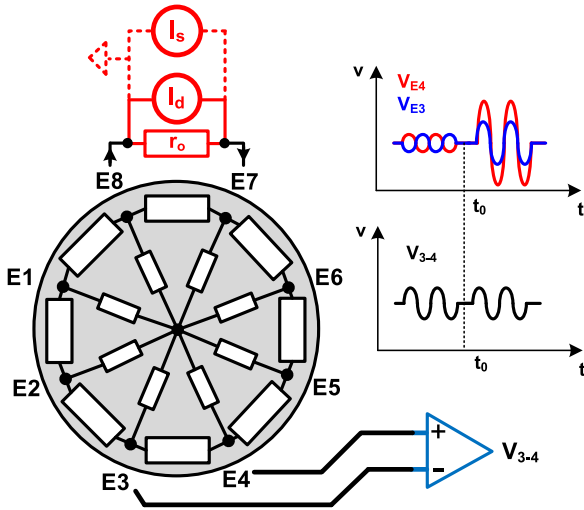In [75], the effect of fractional-N synthesis is also analyzed for the zero-crossing phase detection method to obtain

FIGURE 9. EIT voltage with and without fully differential current drive.

FIGURE 10. EIT fully differential current drive mismatch. (a) Expected matched current source and sink, and (b) common-mode signal due to unmatched current ΔI.

a finer phase resolution using a counter with a moderate clock frequency.

To sum up, I-Q demodulation is the most frequently used approach for EIT (or bioimpedance measurements in general). The I-Q can be implemented using either digital or analog circuits. The mixed-signal approach is a current state-of-the-art implementation in CMOS integrated designs. This approach also explores the use of square waves compared to the single-tone sine for more elegant and efficient circuit design. The magnitude/phase detection method can measure the information directly from the signal waveform. An advantage of the time-to-digital demodulation method is that it merges the readout circuit with digitization instead of using a separate ADC, resulting in a simple and low power design. Depending on the demodulation method, the corresponding circuit implementation can vary considerably. Thus, the choice of demodulation is one of the initial design decisions.

IV. ANALOG FRONT-END CIRCUITS
A. CURRENT INJECTION
A specific requirement for current drivers in EIT systems is to have fully differential outputs. This is to ensure that the common-mode voltage is adequately rejected during measurements. As shown in Fig. 9, the voltage across a target tissue is measured differentially between two electrodes, for example E3 and E4, where the smallest voltages are induced. In the homogeneous resistive mesh shown in the figure, two scenarios are compared; in the first, the system injects a differential current I_d before time t_0 (shown with solid lines), and, in the second scenario after t_0, it switches to single-ended injection I_s with the same current amplitude (shown with dotted lines). While the differential voltage V_{3-4} remains the same (the bottom plot), the common-mode voltage between V_3 and V_4 is significantly larger (the top plot) when using single-ended current I_s compared to the differential current I_d.
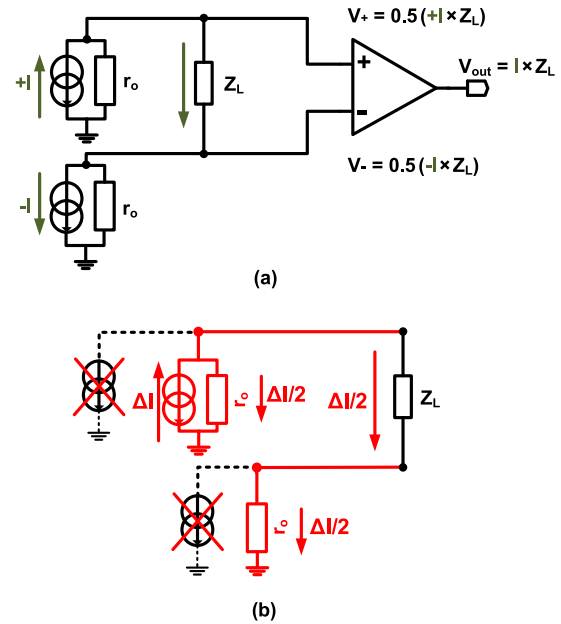
Unlike a voltage output, a fully differential current output is not easily achieved due to unacceptable source and sink current mismatch. As shown in Fig. 10, in a fully differential drive the source and sink current drivers have high output impedances. If there is a mismatch between the source and sink, the mismatch current ΔI has no other return path but to flow to the reference ground through the output impedance. This results in a common-mode voltage $\Delta I(r_o/2)$ (where r_o is the output impedance), which may well saturate the circuit output stage [76].

There are two types of current driver used for bioimpedance measurements. The first type is a DAC-based open-drain current mirror and is a common implementation in CMOS integrated circuit design [69], [70], [74], [77]. It is often used for single-channel impedance measurement rather than EIT applications and utilizes the output drain terminal directly as the current source (PMOS mirror output) or sink (NMOS mirror output). The other type is the voltage-to-current converter (V/I) [20], [47], [68]. When employing current feedback [78], the V/I converter can achieve an accurately defined transconductance (G_m), with a wide bandwidth and high output impedance at the expense of higher power consumption. As discussed in [79] (which reviews various types of current driver), when designing a V/I current driver for EIT, apart from the source-sink mismatch issues, other considerations include bandwidth, phase delays, output impedance and harmonic distortion.

Common-mode feedback (CMFB) is employed to address the source-sink current mismatch [80]. A method to implement CMFB is the inverting unity gain amplifier [81] as shown in Fig. 11. There are two parts to this topology: the master source driver and the slave sink driver. Regardless of
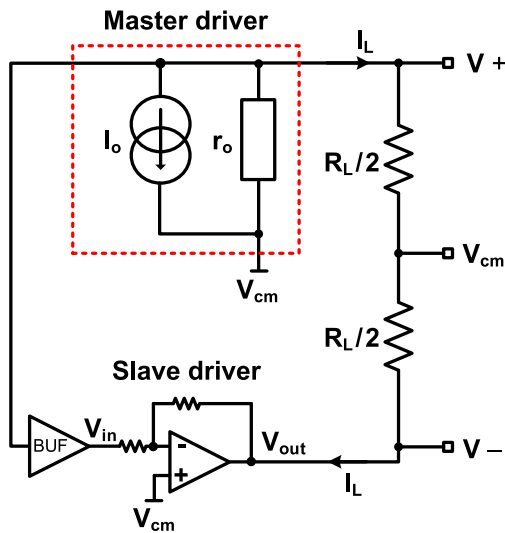
FIGURE 11. EIT fully differential current driver with inverting amplifier implementation.

the master driver design, the slave measures the developed voltage V_+ at the source electrode and generates an inverted signal V_- at the sink electrode. The combination of sink and source currents forms a differential drive or floating current drive; this also biases the body potential to V_{cm} (common-mode voltage) as shown in Fig. 11.

From the CMFB perspective, the opamp measures V_+ and V_- while adjusting its output to achieve a 'virtual short'. This slave circuit can be improved by using a differential difference amplifier (DDA) [82] which provides the inverting amplifier without using an input buffer or resistor [83].

For this topology, the relationship between the master output current I_o, and actual load current I_L is:

$$I_L = I_o \frac{r_o}{r_o + \frac{R_L}{1-A_{cl}}} \qquad (15)$$

where r_o is the master output impedance, R_L is the load and A_{cl} is the closed-loop inverting amplifier gain which should be close to -1. From the above, even though the sink circuit has a voltage output, the current driver still maintains an overall high output impedance.

The common-mode voltage (V_{cm}) for this circuit can be written as:

$$V_{cm} = \frac{V_+ + V_-}{2} = \frac{1}{2} I_L R_L \frac{A_{cl}+1}{A_{cl}-1}. \qquad (16)$$

It can be seen that as A_{cl} tends to -1, the common-mode voltage approaches zero. Frequency-selective CMFB can also be employed to eliminate any noise and interference which may exist in the system [80].

Injection of dc current can lead to electrolysis at the electrode-tissue interface. This is irreversible and can cause tissue damage, therefore ac coupling capacitors are required at the current output. At frequencies higher than 10 Hz, any oxidation or reduction reaction is reversible when the applied

potential is reversed. The ac current injection must comply with the IEC 60601-1 standard to avoid pain, heat generation or undesired muscle contractions. The permissible current is frequency dependent according to the following equation:

$$I = \begin{cases} 100 \ \mu A_{rms} & 0.1 \ Hz < f < 1 \ kHz \\ 100 \frac{f}{1 \ kHz} \ \mu A_{rms} & 1 \ kHz < f < 100 \ kHz \\ 10 \ mA_{rms} & 100 \ kHz < f \end{cases} \qquad (17)$$

where f is the frequency of the injecting current.

The current amplitude in EIT can vary for each application. As a rule of thumb, a larger current provides better SNR for voltage recording, however, due to the electrode contact impedance, a large current injection would require higher voltage compliance leading to a more power-demanding system. In a particular application, a higher current may be required to produce recordable signals on larger circumference subjects when the electrodes are placed far from the current driver.

Finally, the current noise due to the current driver can be seen as another current source in parallel with a load (i.e., the equivalent body impedance). This noise source can be converted to its equivalent voltage noise model, adding it to the recording channel as part of the voltage noise. As the body impedance is low, current noise is often neglected in noise analysis.

B. VOLTAGE ACQUISITION

The voltage acquisition channel consists of two blocks: an instrumentation amplifier (IA), for differential recording, and a programmable-gain amplifier (PGA) for dealing with the 'U'-shaped voltages previously mentioned. As shown earlier in Fig. 1(a), during EIT measurements, the differential voltages at the current-injecting electrodes are ignored because (i) the measured voltage would indicate the contact impedance Z_e (Fig. 2), which is irrelevant to the sample impedance, and (ii) the resulting high-voltage amplitudes would saturate the IAs. Note that a useful and practical approach that benefits from rotational injection could be that the voltages measured at the current-injecting electrodes, either single-ended or differential, can be compared with an expected threshold to determine the electrode contact conditions [47].

For the IA design, the key EIT-related considerations are the common-mode rejection ratio (CMRR) and input/output linear range. Because of the 'U'-shaped voltage pattern, even excluding the injecting electrodes, the IA must have a wide input linear range. As an example, in lung imaging, the maximum voltage could be 60-70 dB higher than the minimum voltage [19]. The dynamic range depends on the circumference of the object under test as well as the electrode spacing. Amplification is required in the first stage of the IA for higher SNR, and its output stage must not be saturated due to the wide input dynamic range. One solution is to use dynamic current injection that equalizes the voltage levels [15], [20].

The CMRR is especially important because EIT measures the changes in differential voltages. Commercial IAs typically have a CMRR of 60-70 dB at around 50 kHz, while advanced CMOS implementations can achieve in excess of 80 dB at 1 MHz [19], [84]. However, the CMRR degrades when faced with unbalanced input coupling, for example, due to long cables between the electrodes and the IA inputs. Placing the IA close (< 5 cm) to the electrode pad (i.e., to form an 'active electrode' (AE)) would have the following benefits: (i) higher CMRR, (ii) stable input impedance, and (iii) reduced noise coupling. AEs have been employed in recent state-of-the-art CMOS EIT designs [19], [20].

The design of IAs usually follows a standard three opamp configuration in discrete circuits. However, it varies in CMOS integrated solutions. Two commonly encountered IA designs in integrated EIT systems are the current feedback IA (CFIA) [86] and the resistive feedback IA (RFIA) [68] as shown in Fig. 12 (which could also be a capacitive feedback IA [87]). The working principle of CFIA can be found in [88] and the CMRR analysis for CFIA is detailed in [85]. Variations of this design could be CMRR enhancement feedback loop [19], and a wide bandwidth (10 MHz) design [9]. The gain of both the CFIA and RFIA can be set using resistance ratios. The linear range of the RFIA can be close to the supply rail due to the voltage feedback, whereas for the CFIA, it is defined by $2 \cdot R_i \cdot I_{P1}$ with reference to Fig. 12(a). Compared to the use of multiple copies of the bias current in the CFIA, the implementation of the RFIA is much simpler, and thus requires less power. However, due to the balanced topology, the CFIA is likely to achieve a much higher CMRR.

Fig. 12 shows two approaches of merging square wave demodulation into the output of the IA (by chopping $f_{chop} = f_{I/Q}$). In Fig. 12(a), chopping is at the output stage so that the CFIA can maintain its high input impedance, whereas in the design shown in Fig. 12(b), the chopping is prior to the IA. Here, the signal is down-converted into the baseband while the dc electrode offset is up-modulated. With the signal in the baseband, the RFIA can be designed with a lower bandwidth, and hence, lower power consumption. Nonetheless, this has the disadvantage of a lower input impedance which is defined as:

$$Z_{in-dc} = \frac{1}{C_{in}f_{chop}} // R_1 \qquad (18)$$

where C_{in} is the input capacitance. An input impedance boosting technique can be found in [89].

Achieving a 'full-ADC' range for every channel may be impractical. As a result, a PGA is implemented after the IA stage to equalize the 'U'-shaped voltage levels across the different electrodes. One design consideration is to decide on the required gain levels for the PGA. A second consideration is the question of whether to have an automatic gain adjustment, which may cause delays in the EIT scan speed, or whether to set the gains according to a lookup table (LUT). The LUT method is effective for a targeted
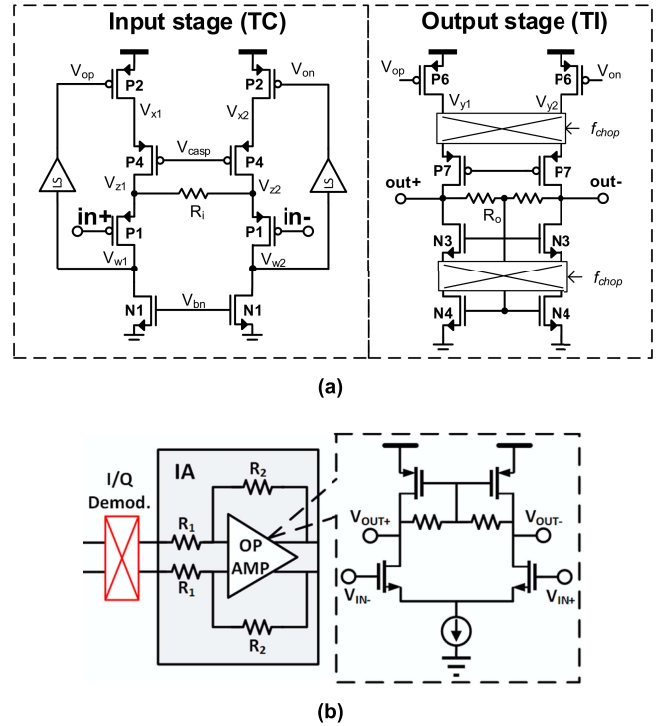

(a)

(b)

FIGURE 12. (a) Current feedback IA [86] and (b) resistive feedback IA [68].

application because the 'U' shape gives a good indication of the level of gain required for the voltages from each electrode pair.

V. INTEGRATED EIT SYSTEMS

Many EIT systems currently in the research and development stage are (at least partly) implemented on chip toward the goal of miniaturization to facilitate wearability, portability and/or low power consumption. In this section a number of recently published integrated designs from 2017 to 2020 are reviewed. The most recent are discussed first.

In 2020, Rao *et al.* [43] presented a 16-electrode EIT system for prostate imaging using a 4×5 grid of flexible sonolucent electrode array in combination with a transrectal ultrasound probe and a biopsy needle providing EIT imaging during the biopsy process. Four channels are implemented on one chip, each of which includes a current generator and an analog front-end for bioimpedance measurement. Also, out of the twenty channels, four are used for testing purposes and therefore the system has sixteen functional channels. A current-conveyor-based current driver (described in [90]) receives its sinusoidal input voltage generated by an off-chip DDS. As shown in Fig. 13, the sinewave voltage (V_Y) is fed into a transconductance amplifier, the output of which is buffered to the node V_X via a class AB stage, and, as a result, V_Y converts to I_X. This current is further amplified in a following gain-boosted cascode stage which helps to achieve a high output impedance. The input transconductor is a two-stage amplifier that uses the indirect compensation technique splitting the poles while eliminating the right
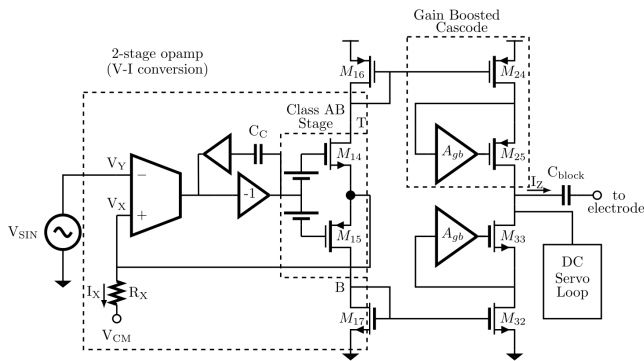
FIGURE 13. The current driver in [43].

half-plane zero that would be introduced in the conventional Miller compensation. This compensation method benefits from a lower capacitance and does not restrict the bandwidth. Furthermore, a dc servo loop is used to stabilize the output common-mode voltage. A total harmonic distortion (THD) of 0.15% is reported for the generated current when its amplitude and frequency are at maximum (1 mA$_{p-p}$ and 1 MHz, respectively). The voltage readout IA is based on [22] using the current feedback topology previously mentioned with a resistor ladder at the output stage of the PGA. Fully digital I-Q demodulation is subsequently performed on an FPGA following ADC conversion using a 10-bit 250 kSPS successive-approximation register (SAR). Each of the four chips was fabricated in a 180 nm CMOS process and the overall system has a frame rate of 10 fps, with a bandwidth of 1 MHz and a power consumption of 90 mW.

An eight-electrode EIT system for breast cancer detection was designed by Lee *et al.* in 2020 which is capable of image reconstruction on a mobile imaging application [48]. The design exploits a reconfigurable front-end structure which can be used in both current driver and voltage sensor modes (Fig. 14). For the sensing circuit, a wide dynamic-range low-noise amplifier (WDR-LNA) is designed by cascading a transconductance and a transimpedance amplifier in the signal path and using another narrow-band transimpedance amplifier in a feedback loop to provide ac coupling without contributing much noise to the circuit. The designed WDR-LNA is based on the CFIA with chopping I-Q demodulation and exhibits a gain of 24 dB, an input-referred noise of 14.2 nV/$\sqrt{}$Hz for a 1 kHz-10 MHz bandwidth and a dynamic range of 120 dB. As seen in Fig. 14(b), the current driver injects the current through two opamps, one of which is used to apply a reference voltage to the electrode and the other provides an amplification to a sine signal. The phase of this signal is adjusted in a phase compensation loop (PCL) using a technique proposed in [91] to reduce the phase error. During the current driver mode, the current flow is monitored through the WDR-LNA in the same AE and after I-Q demodulation, two dc voltages are generated based on the amplitude and phase of the measured voltage. The I and Q dc voltages are then compared with V_{CTRL} and V_{REF} voltages, respectively, and the adjusted voltages are translated
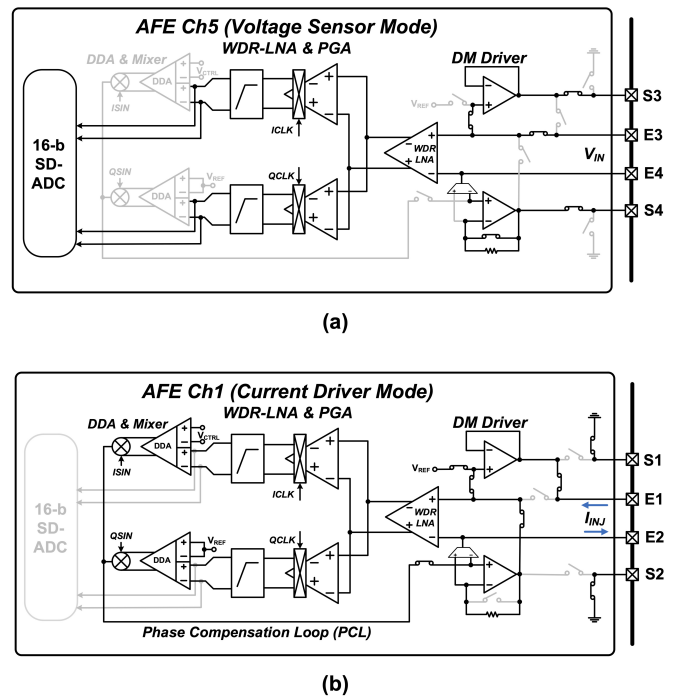

(a)

(b)

FIGURE 14. The reconfigurable front-end in [48] configured in (a) voltage sensor mode and (b) current driver mode.

into a sinusoidal signal through two active mixers. Finally, the generated sinewave with the modified phase is fed into the current driver opamp for current injection to the tissue. This structure results in a 4.32° phase error at 10 MHz, which, according to the paper, would have been 58° without using the PCL. A maximum current of 3 mA$_{p-p}$ within a bandwidth of 10 kHz-10 MHz can be generated using this design. The system occupies an area of 16 mm^2 in a 65 nm CMOS technology and consumes 9.6 mW per channel.

Liu *et al.* [68] reported a 16-electrode EIT system in 2019 for lung imaging where one pair of injecting electrodes and 13 pairs of sensing electrodes can be selected at a time using a switching network. An LUT provides a sinusoidal signal with four tunable frequencies (15.625, 31.25, 62.5 and 125 kHz) and amplitudes. The resulting sine signal is fed to a V/I converter through a DAC and low-pass filtering. The V/I converter employs a tunable resistor so that together with the four amplitude sinewaves stored in the LUT, the current driver encompasses 16 programmable steps varying from 20 μA to 200 μA. For the recording, an early I-Q demodulating chopper amplifier is utilized before any amplification stage in each of the thirteen voltage-sensing channels to transfer the recorded signal to the baseband. Frequency-division multiplexing (FDM) is used to transfer the recorded signals from all channels to a computer through a USB cable 'in one go' while at the same time allowing all thirteen channels to be digitized simultaneously with two parallel ADCs and eliminating the need for multiplexing. This is realized by the method shown in Fig. 15, where the amplified baseband signals from each channel are modulated to a higher frequency between 5.1 kHz and 8.7 kHz with
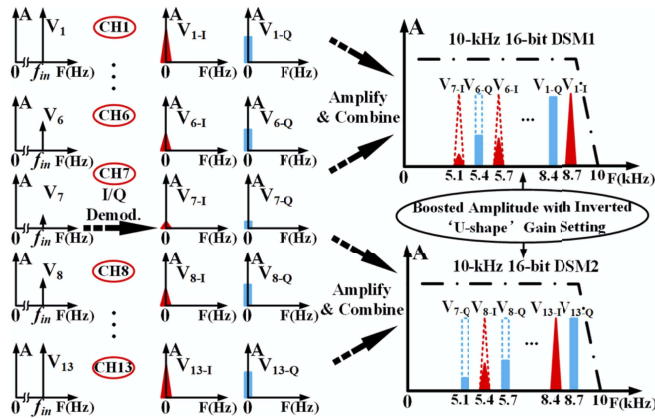
FIGURE 15. The frequency division multiplexing (FDM) technique in [68].

300 Hz spacing steps. Subsequently, the I and Q signals from all the channels are combined together and sent to a computer after digitization using two delta-sigma modulators (DSMs) with a 4 MHz sampling rate that supports an overall 10 kHz signal bandwidth. The I-Q information for each channel can be recovered by applying a fast Fourier transform (FFT) algorithm to the output of the DSMs. The chip was implemented in a 130 nm CMOS technology, occupying an area of 11.2 mm^2 and consuming a total power of 1.53 mW with a 1 V supply voltage. The system has an SNR of 53.3 dB, a bandwidth of 125 kHz and an image frame rate of 5 fps.

In 2019 Wu *et al.* [20] presented a wearable 16-electrode EIT belt with AE chips for neonatal thorax vital sign monitoring as shown in Fig. 16(a). The sink and source current drivers provide a current of up to 6 mA and are connected in a current-mode CMFB configuration to minimize any common-mode signal. Unlike the conventional AE EIT architecture with front-end buffers on the recording side, this system features IAs directly coupled to the electrodes without multiplexing for maximum CMRR, as shown in Fig. 16(b). With the support of a summation readout topology (V_{sum}), it also allows differential voltages to be recorded from any selected pair of electrodes offering maximum flexibility in EIT recording. Each MUX4 switch is used to select or de-select the respective IA output, for example, in Fig. 16(b), $V_{sum} = V_{E11} - V_{E8}$. To operate the AEs, a central hub was implemented using an FPGA and discrete components. The FPGA has a 12-bit LUT to generate sinewaves with programmable frequencies of 125 kHz, 250 kHz, 500 kHz and 1 MHz. The generated sinewave is converted to analog using a 12-bit DAC (at 32 MSPS) which is then transferred to the input of a current driver in one of the 16 AEs. The recorded voltage from the AEs is further amplified through the PGAs in the central hub, sent to a 12-bit ADC, transferred to a digital I-Q demodulator, and finally sent to a computer via an Ethernet interface. The AEs were implemented in a 350 nm high-voltage technology with ±9 V analog and ±3 V digital supply voltages. Each AE consumes a maximum power of 250 mW, and the total area is 9.61 mm^2. The system supports up to 1 MHz of bandwidth and a frame rate of 122 fps with a 54.3 dB SNR.
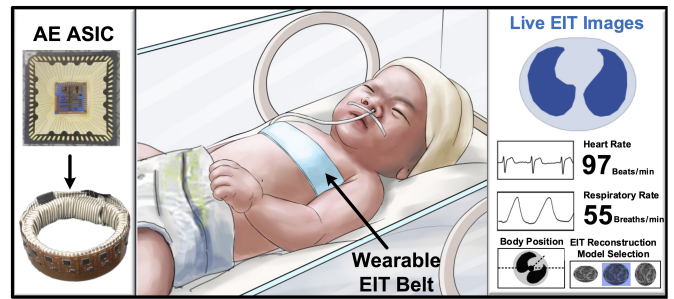
(a)
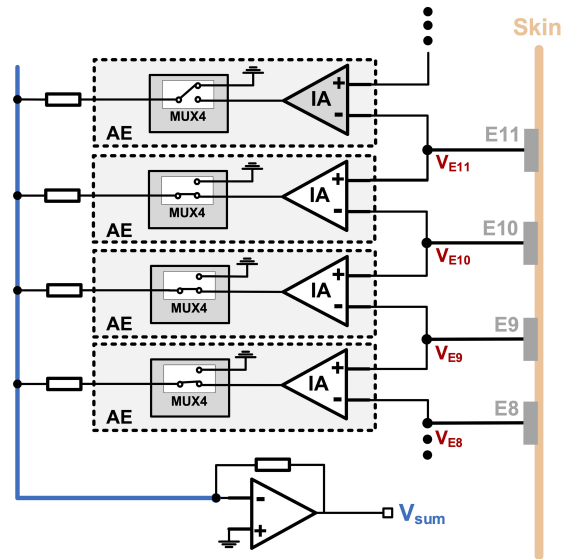
(b)

FIGURE 16. The multisensory wearable EIT belt in [20] with AEs for neonatal thorax vital sign monitoring. (a) Concept design and belt implementation with ASICs. (b) Summation readout architecture for AEs.

In 2018 Xu *et al.* [77] presented a multifunctional brain monitoring device with sixteen active sensor chips, each containing three modules for performing electroencephalography (EEG), EIT and near-infrared spectroscopy (NIRS) on the scalp. The EIT section mainly consists of a current driver and a bioimpedance readout circuit. The current generator enables a square-wave current to be injected to (or collected from) the tissue via a "chopper-stabilized bandgap reference generator" to reduce the $1/f$ noise. This can provide a current of 5 µA to 100 µA within a frequency range of 1 kHz to 1 MHz. The bioimpedance recording repeats sequentially among all pairs of AEs. The readout circuit provides a dynamic gain between 20 V/V to 200 V/V and mainly includes a transimpedance amplifier with an analog dc servo loop to remove the dc offset (instead of a high-pass filter) and two in-phase and quadrature-phase transimpedance amplifiers. As shown in Fig. 17, the extraction of I and Q 'BioZ' signals takes place after a first stage amplification based on the merged I-Q chopping approach mentioned

previously. This is implemented by multiplying the signal by $f_{IMP(90)}$-f_c and $f_{IMP(0)}$-f_c, which also transfers the BioZ to dc and results in (i) improving the input impedance of the readout circuit, (ii) reducing power consumption by the following transimpedance stages, and (iii) shifting the amplifier's $1/f$ noise out of the band (to the chopping frequency). The I and Q signals are digitized using two 12-bit SAR ADCs. The entire EEG/EIT/NIRS active sensor was implemented on a 16 mm^2 chip using a 180-nm CMOS technology. With a 1.2 V power supply, the EIT readout and current generator blocks consume 45 μW and 25 μW of power (for 20 μA current), respectively, and a 3 m$\Omega/\sqrt{Hz}$ impedance sensitivity was reported for this system.

Finally, in 2017 Kim *et al.* [19] reported a 48-channel 3D EIT belt with AEs for lung ventilation monitoring. Inside each AE there is a current driver, an impedance readout circuit and a digital block for EIT operation. The system uses both time-difference and frequency-difference imaging methods, the latter is useful for imaging temporal changes in the tissue while the former is mostly suitable for static imaging and boundary extraction. To ensure that the optimum frequency with the largest impedance difference is chosen in every individual patient, the maximum length sequence (MLS) method is used at the beginning of the measurement. A 256 kHz pseudorandom binary sequence (PRBS) with an even power spectrum with some frequency gaps, is injected into the tissue. The cross correlation of the measured voltage with the applied input represents the system's transfer function. It can use to detect the two frequencies for frequency-difference imaging at which the highest impedance variation can be observed. The sine signal for both frequency-difference and time-difference EIT is generated using a pseudo-sine generator and shares a 6-bit DAC and a current driver with the PRBS generator unit (both are stored in LUTs). The current driver is implemented with current feedback topology and can generate four programmable current levels up to 1 mA within a frequency range of 10 kHz to 256 kHz and with a THD less than 0.5% at 128 kHz. The core of the readout front-end is based on a CFIA that uses a fully differential tri-loop structure shown in Fig. 18, where: (i) the dc servo loops are designed to remove output dc offsets by integration, (ii) a boosting loop is used to improve the CMRR by averaging the output common-mode voltage and canceling it from the input, and (iii) a fast-settling loop is utilized to speed up the processing time and make the system compatible for 10 fps acquisition. The authors reported a CMRR between 93 dB and 108 dB at 300 kHz, a noise floor of 21 nV/$\sqrt{Hz}$ and a 1% THD for inputs greater than 50 mV$_{p-p}$. The data is then converted to digital using a 12-bit SAR ADC with a sampling frequency of 256 kHz during MLS mode and 10 kHz otherwise. The overall system has a power consumption of 6.96 mW for sixteen electrodes. Each AE and the central hub were fabricated in a 65 nm CMOS technology with an area of 3.19 mm^2 and 1.26 mm^2, respectively.
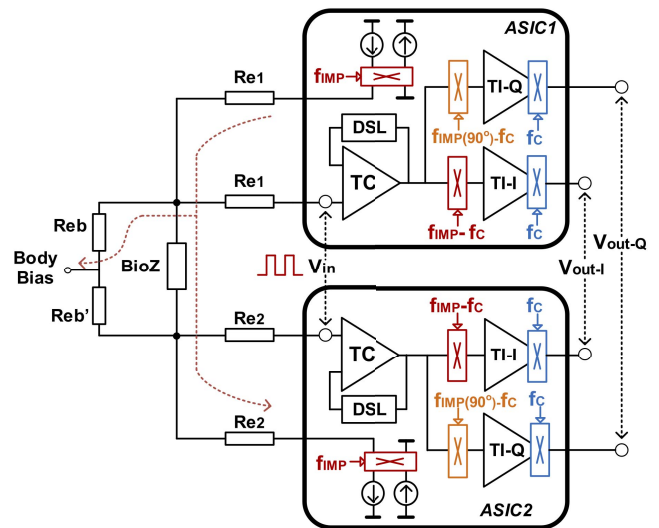

FIGURE 17. The analog front-end AE in [77].

Note that the noise characterization discussed in this section focuses on the recording front-end; however, the current driver also contributes to the overall EIT noise performance. As mentioned in Section IV-A, current noise is usually neglected because the load that the current noise acts upon varies in bioimpedance recordings, and more importantly, the recording front-end noise often dominates the noise performance.

Table 1 summarizes the performance of the six integrated EIT systems reviewed in this section. The designs in [43] and [20] are more power consuming compared to the other. Note that [20] uses a high-voltage technology with a ±9 V supply and a maximum of 6 mA current, while [43] consumes 90 mW power per channel for a maximum of 1.2 mA current generation with a 3.3 V power supply. Although both these systems use digital I-Q demodulation, analog demodulation is used in the other integrated systems in Table 1.

The SNR used in Table 1 is defined as:

$$\text{SNR}_i = \left(\frac{\sum_{n=1}^{N} V_n}{\sum_{n=1}^{N} \left| V_n - \overline{V_N} \right|} \right)_i$$

$$\overline{\text{SNR}_{dB}} = 20\log_{10} \frac{1}{ch_{max}} \sum_{i=1}^{ch_{max}} \text{SNR}_i \qquad (19)$$

where ch_{max} is the total number of measurement channels, e.g., for an EIT system with x electrodes, $ch_{max} = x(x-3)$ and SNR_i is calculated for each channel. N is the total number of frames measured for the calculation, V_n is the measured channel voltage and $\overline{V_n}$ is the average voltage measured within channel i over N frames. $\overline{\text{SNR}_{dB}}$ represents the system measurement repeatability and is commonly used in multiple EIT systems reported in the literature [9], [20], [87], [92], [93].

VI. CHALLENGES AND FUTURE DIRECTIONS
Despite a relatively large number of publications on EIT systems, they are not yet widely used by clinicians across the many biomedical applications. As of the date of this

TABLE 1. Performance of published integrated EIT systems.

Ref.	Application	Demodulation method	Signal waveform	Number of channels	Power per channel (mW)	Maximum current (mA)	Frame rate (fps)	Bandwidth (Hz)	SNR[a] (dB)
[43]	Prostate cancer screening	Digital	Sine	16	90	1.2	10	100 – 10M	66 – 76
[48]	Breast cancer screening	Analog	Sine	8	9.6	3	NA	10k – 10M	NA
[68]	Lung imaging	Analog	16-tone tunable sine	13	0.118	0.2	5	125k	53.3
[20]	Neonatal thorax monitoring	Digital	4-tone tunable sine	16	250	6	122	45k – 1M	54.3[b]
[77]	Functional brain imaging	Analog	Square	15	0.665	0.2	NA	1M	NA
[19]	3D lung ventilation monitoring	Analog	Pseudo-sine	48	0.145	1	10	256k	NA

[a]SNR as defined in Eq. (19); [b]at 125 kHz.
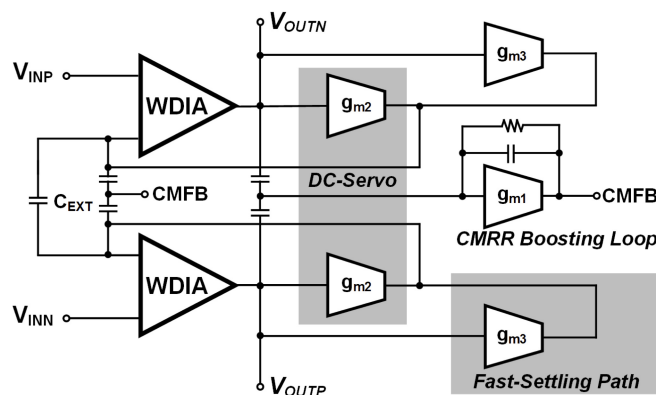
FIGURE 18. The front-end IA in [19].

review, more than 1,700 publications on EIT are listed in the MEDLINE/PubMed database and around 80 published clinical trials.

A recent study on the use of EIT in pediatric intensive care has investigated different scenarios such as asthma, targeted physiotherapy and positive end-expiratory pressure optimization, where EIT can provide unique information that cannot be collected by other modes of monitoring [18]. There are several commercial EIT systems already available on the market, for example, SenTec LuMon, Maltron Sheffield MK 3.5 and Dräger's PulmoVista 500 that offer EIT in daily clinical practice for lung function monitoring.

However, barriers remain that hinder the widespread use of EIT by clinicians. These include, for example, having to deal with an extra device connected to the patient, and the additional maintenance and care required to ensure that suitable contacts between the device electrodes and the skin are always in place. Although EIT has the potential to become an inexpensive monitoring technique, in contrast to emerging low-power, wireless and miniaturized research-based devices, the available commercial EIT systems are bulky in size and inefficient in power consumption. Also, the transfer of collected data to a processing computer for image reconstruction is via a cable, which all hinder portable monitoring and restrict the patient's movement.

To further motivate physicians to include EIT in their clinical routines, development should be concentrated on bridging the gap between the commercialized and research-based state-of-the-art systems. Given the unique advantages that EIT offers in real-time monitoring of clinical status, a successful outcome can be envisaged for the adoption of EIT provided that a number of avenues are further explored. As discussed in [94], there should be development of universal guidelines specifying how EIT information could be incorporated in diagnostic and therapeutic plans for different conditions [8]. In addition, technical steps such as technology standardization [95], provision of commercial EIT microchips, and employment of artificial intelligence in algorithms to improve image resolution should be considered for future EIT devices.

VII. CONCLUSION

This paper has provided a review of the underlying principles of EIT system design and various biomedical applications. Furthermore, a number of the commonly used design architectures for current drivers, analog front-end circuits and demodulation methods have been discussed in detail with possible tradeoffs. In the context of current biomedical utilizations, state-of-the-art integrated implementations have been subsequently described to illustrate hardware design approaches and challenges in their realization together with different system evaluation considerations. Resolution of the limitations of the present commercial EIT systems preventing widespread clinical use has been discussed. Given the high potential of the EIT technique for providing a low-cost, radiation-free, real-time and wearable means for physiological status monitoring, translation into the clinic is in need of further development and is of current importance.

REFERENCES

[1] D. C. Barber and B. H. Brown, "Applied potential tomography," *J. Phys. E, Sci. Instrum.*, vol. 17, no. 9, p. 723, 1984.

[2] B. M. Eyuboglu, B. H. Brown, and D. C. Barber, "In vivo imaging of cardiac related impedance changes," *IEEE Eng. Med. Biol. Mag.*, vol. 8, no. 1, pp. 39–45, Mar. 1989.

[3] I. Frerichs, "Electrical impedance tomography (EIT) in applications related to lung and ventilation: A review of experimental and clinical activities," *Physiol. Meas.*, vol. 21, no. 2, pp. R1–R21, 2000.

[4] B. H. Brown, "Electrical impedance tomography (EIT): A review," *J. Med. Eng. Technol.*, vol. 27, no. 3, pp. 97–108, 2003.

[5] C. Putensen, B. Hentze, S. Muenster, and T. Muders, "Electrical impedance tomography for cardio-pulmonary monitoring," *J. Clin. Med.*, vol. 8, no. 8, p. 1176, 2019.

[6] C. L. Yang, "Electrical impedance tomography: Algorithms and applications," Ph.D. dissertation, Dept. Elect. Electron. Eng., Univ. Bath, Bath, U.K., 2014.

[7] R. Bayford and A. Tizzard, "Bioimpedance imaging: An overview of potential clinical applications," *Analyst*, vol. 137, no. 20, pp. 4635–4643, 2012.

[8] I. Frerichs et al., "Chest electrical impedance tomography examination, data analysis, terminology, clinical use and recommendations: Consensus statement of the TRanslational EIT developmeNt stuDy group," *Thorax*, vol. 72, no. 1, pp. 83–93, 2017.

[9] M. Takhti, Y.-C. Teng, and K. Odame, "A 10 MHz read-out chain for electrical impedance tomography," *IEEE Trans. Biomed. Circuits Syst.*, vol. 12, no. 1, pp. 222–230, Feb. 2018.

[10] S. F. Khalil, M. S. Mohktar, and F. Ibrahim, "The theory and fundamentals of bioimpedance analysis in clinical status monitoring and diagnosis of diseases," *Sensors*, vol. 14, no. 6, pp. 10895–10928, 2014.

[11] Ø. G. Martinsen, B. Nordbotten, S. Grimnes, H. Fossan, and J. Eilevstjønn, "Bioimpedance-based respiration monitoring with a defibrillator," *IEEE Trans. Biomed. Eng.*, vol. 61, no. 6, pp. 1858–1862, Jun. 2014.

[12] W. Lee and S. Cho, "Integrated all electrical pulse wave velocity and respiration sensors using bio-impedance," *IEEE J. Solid-State Circuits*, vol. 50, no. 3, pp. 776–785, Mar. 2015.

[13] A. Adler et al., "Whither lung EIT: Where are we, where do we want to go and what do we need to get there?" *Physiol. Meas.*, vol. 33, no. 5, pp. 679–694, 2012.

[14] M. C. Bachmann et al., "Electrical impedance tomography in acute respiratory distress syndrome," *Crit. Care*, vol. 22, no. 1, p. 263, 2018.

[15] J. Lee, U. Ha, and H.-J. Yoo, "30-fps SNR equalized electrical impedance tomography IC with fast-settle filter and adaptive current control for lung monitoring," in *Proc. IEEE Int. Symp. Circuits Syst. (ISCAS)*, Montreal, QC, Canada, 2016, pp. 109–112.

[16] V. Tomicic and R. Cornejo, "Lung monitoring with electrical impedance tomography: Technical considerations and clinical applications," *J. Thorac. Dis.*, vol. 11, no. 7, p. 3122, 2019.

[17] Y. Lee, K. Song, and H.-J. Yoo, "A 4.84mW 30fps dual frequency division multiplexing electrical impedance tomography SoC for lung ventilation monitoring system," in *Proc. Symp. VLSI Circuits (VLSI Circuits)*, Kyoto, Japan, 2015, pp. C204–C205.

[18] P. Davies, S. Yasin, S. Gates, D. Bird, and C. Silvestre, "Clinical scenarios of the application of electrical impedance tomography in paediatric intensive care," *Sci. Rep.*, vol. 9, no. 1, p. 5362, 2019.

[19] M. Kim et al., "A 1.4-mΩ sensitivity 94-dB dynamic-range electrical impedance tomography SoC and 48-channel hub-SoC for 3-D lung ventilation monitoring system," *IEEE J. Solid-State Circuits*, vol. 52, no. 11, pp. 2829–2842, Nov. 2017.

[20] Y. Wu, D. Jiang, A. Bardill, R. Bayford, and A. Demosthenous, "A 122 fps, 1 MHz bandwidth multi-frequency wearable EIT belt featuring novel active electrode architecture for neonatal thorax vital sign monitoring," *IEEE Trans. Biomed. Circuits Syst.*, vol. 13, no. 5, pp. 927–937, Oct. 2019.

[21] A. A. Colin, C. McEvoy, and R. G. Castile, "Respiratory morbidity and lung function in preterm infants of 32 to 36 weeks' gestational age," *Pediatrics*, vol. 126, no. 1, pp. 115–128, 2010.

[22] A. Rao et al., "An analog front end ASIC for cardiac electrical impedance tomography," *IEEE Trans. Biomed. Circuits Syst.*, vol. 12, no. 4, pp. 729–738, Aug. 2018.

[23] H. Ross, "Technical developments to enable electrical impedance tomography (EIT) measurement of blood flow to monitor cardiac output: key engineering contributions," M.S. thesis, Dept. Syst. Comput. Eng., Carleton Univ., Ottawa, ON, Canada, 2010.

[24] R. Pikkemaat, S. Lundin, O. Stenqvist, R.-D. Hilgers, and S. Leonhardt, "Recent advances in and limitations of cardiac output monitoring by means of electrical impedance tomography," *Anesth. Analgesia*, vol. 119, no. 1, pp. 76–83, 2014.

[25] S. Zlochiver, D. Freimark, M. Arad, A. Adunsky, and S. Abboud, "Parametric EIT for monitoring cardiac stroke volume," *Physiol. Meas.*, vol. 27, no. 5, pp. S139–S146, 2006.

[26] R. P. Patterson, J. Zhang, L. I. Mason, and M. Jerosch-Herold, "Variability in the cardiac EIT image as a function of electrode position, lung volume and body position," *Physiol. Meas.*, vol. 22, no. 1, pp. 159–166, 2001.

[27] S. H. Arshad, J. S. Kunzika, E. K. Murphy, K. Odame, and R. J. Halter, "Towards a smart phone-based cardiac monitoring device using electrical impedance tomography," in *Proc. IEEE Biomed. Circuits Syst. Conf. (BioCAS)*, Atlanta, GA, USA, 2015, pp. 1–4.

[28] A. Hasan and V. Paul, "Telemonitoring in chronic heart failure," *Eur. Heart J.*, vol. 32, no. 12, pp. 1457–1464, 2011.

[29] J. Avery, T. Dowrick, M. Faulkner, N. Goren, and D. Holder, "A versatile and reproducible multi-frequency electrical impedance tomography system," *Sensors*, vol. 17, no. 2, p. 280, 2017.

[30] A. T. Tidswell, "Functional electrical impedance tomography of adult and neonatal brain function," Ph.D. dissertation, Dept. Med. Phys. Biomed. Eng., Univ. Coll. London, London, U.K., 2006.

[31] D. S. Holder, "Electrical impedance tomography (EIT) of brain function," *Brain. Topogr.*, vol. 5, no. 2, pp. 87–93, 1992.

[32] F. Fu et al., "Use of electrical impedance tomography to monitor regional cerebral edema during clinical dehydration treatment," *PLoS ONE*, vol. 9, no. 12, 2014, Art. no. e113202.

[33] H. Mestre et al., "Cerebrospinal fluid influx drives acute ischemic tissue swelling," *Science*, vol. 367, no. 6483, 2020, Art. no. eaax7171.

[34] Z. Xu et al., "Development of a portable electrical impedance tomography system for biomedical applications," *IEEE Sensors J.*, vol. 18, no. 19, pp. 8117–8124, Oct. 2018.

[35] T. Tang, M. D. Weiss, P. Borum, S. Turovets, D. Tucker, and R. Sadleir, "In vivo quantification of intraventricular hemorrhage in a neonatal piglet model using an EEG-layout based electrical impedance tomography array," *Physiol. Meas.*, vol. 37, no. 6, pp. 751–764, 2016.

[36] G. W. Crile, H. R. Hosmer, and A. F. Rowland, "The electrical conductivity of animal tissues under normal and pathological conditions," *Amer. J. Physiol.*, vol. 60, no. 1, pp. 59–106, 1922.

[37] B. Blad and B. Baldetorp, "Impedance spectra of tumour tissue in comparison with normal tissue; a possible clinical application for electrical impedance tomography," *Physiol. Meas.*, vol. 17, pp. A105–A115, Nov. 1996.

[38] R. Pethig, "Dielectric properties of biological materials: Biophysical and medical applications," *IEEE Trans. Electr. Insul.*, vol. EI-19, no. 5, pp. 453–474, Oct. 1984.

[39] R. Lee et al., "Dielectric imaging for differentiation between cancer and inflammation in vivo," *Sci. Rep.*, vol. 7, no. 1, 2017, Art. no. 13137.

[40] Y. Wan et al., "Transrectal electrical impedance tomography of the prostate: Spatially coregistered pathological findings for prostate cancer detection," *Med. Phys.*, vol. 40, no. 6, 2013, Art. no. 63102.

[41] W. J. Catalona et al., "Comparison of digital rectal examination and serum prostate specific antigen in the early detection of prostate cancer: Results of a multicenter clinical trial of 6,630 men," *J. Urol.*, vol. 197, no. 2S, pp. S200–S207, 2017.

[42] A. Borsic, R. Halter, Y. Wan, A. Hartov, and K. D. Paulsen, "Electrical impedance tomography reconstruction for three-dimensional imaging of the prostate," *Physiol. Meas.*, vol. 31, no. 8, pp. S1–S16, 2010.

[43] A. Rao, E. K. Murphy, R. J. Halter, and K. M. Odame, "A 1 MHz miniaturized electrical impedance tomography system for prostate imaging," *IEEE Trans. Biomed. Circuits Syst.*, vol. 14, no. 4, pp. 787–799, Aug. 2020.

[44] H. Syed, A. Borsic, A. Hartov, and R. J. Halter, "Anatomically accurate hard priors for transrectal electrical impedance tomography (TREIT) of the prostate," *Physiol. Meas.*, vol. 33, no. 5, pp. 719–738, 2012.

[45] R. A. Hubbard, K. Kerlikowske, C. I. Flowers, B. C. Yankaskas, W. Zhu, and D. L. Miglioretti, "Cumulative probability of false-positive recall or biopsy recommendation after 10 years of screening

mammography: A cohort study," *Ann. Intern. Med.*, vol. 155, no. 8, pp. 481–492, 2011.

[46] M. T. Le, C. E. Mothersill, C. B. Seymour, and F. E. McNeill, "Is the false-positive rate in mammography in North America too high?" *Brit. J. Radiol.*, vol. 89, no. 1065, 2016, Art. no. 20160045.

[47] S. Hong *et al.*, "A 4.9 mΩ-sensitivity mobile electrical impedance tomography IC for early breast-cancer detection system," *IEEE J. Solid-State Circuits*, vol. 50, no. 1, pp. 245–257, Jan. 2015.

[48] J. Lee *et al.*, "A 9.6 mW/Ch 10 MHz wide-bandwidth electrical impedance tomography IC with accurate phase compensation for breast cancer detection," in *Proc. IEEE Custom Integr. Circuits Conf. (CICC)*, Boston, MA, USA, 2020, pp. 1–4.

[49] V. Cherepenin *et al.*, "A 3D electrical impedance tomography (EIT) system for breast cancer detection," *Physiol. Meas.*, vol. 22, no. 1, pp. 9–18, 2001.

[50] A. A. Amin, S. Parvin, M. A. Kadir, T. Tahmid, S. K. Alam, and K. Siddique-e Rabbani, "Classification of breast tumour using electrical impedance and machine learning techniques," *Physiol. Meas.*, vol. 35, no. 6, pp. 965–974, 2014.

[51] H. Wu, W. Zhou, Y. Yang, J. Jia, and P. Bagnaninchi, "Exploring the potential of electrical impedance tomography for tissue engineering applications," *Materials*, vol. 11, no. 6, p. 930, 2018.

[52] B. Elleby, L. F. Knudsen, B. H. Brown, C. E. Crofts, M. J. Woods, and E. A. Trowbridge, "Electrical impedance assessment of muscle changes following exercise," *Clin. Phys. Physiol. Meas.*, vol. 11, no. 2, pp. 159–166, 1990.

[53] D. Naranjo-Hernández, J. Reina-Tosina, and M. Min, "Fundamentals, recent advances, and future challenges in bioimpedance devices for healthcare applications," *J. Sens.*, vol. 2019, Jul. 2019, Art. no. 9210258. [Online]. Available: https://www.hindawi.com/journals/js/2019/9210258/

[54] D. L. Duren *et al.*, "Body composition methods: Comparisons and interpretation," *J. Diabetes Sci. Technol.*, vol. 2, no. 6, pp. 1139–1146, 2008.

[55] J. D. Hirschman and J. A. Kresge, "Synthesis of a symposium: Innovative non- or minimally-invasive technologies for monitoring health and nutritional status in mothers and young children," *J. Nutr.*, vol. 131, no. 5, pp. 1643S–1645S, 2001.

[56] Y. Nakae, H. Onouchi, M. Kagaya, and T. Kondo, "Effects of aging and gastric lipolysis on gastric emptying of lipid in liquid meal," *J. Gastroenterol.*, vol. 34, no. 4, pp. 445–449, 1999.

[57] Y. Wu, D. Jiang, J. Duan, X. Liu, R. Bayford, and A. Demosthenous, "A human–machine interface using electrical impedance tomography for hand prosthesis control," *IEEE Trans. Biomed. Circuits Syst.*, vol. 12, no. 6, pp. 1322–1333, Dec. 2018.

[58] S. Hannan, M. Faulkner, K. Aristovich, J. Avery, and D. Holder, "Investigating the safety of fast neural electrical impedance tomography in the rat brain," *Physiol. Meas.*, vol. 40, no. 3, 2019, Art. no. 034003.

[59] A. Adler *et al.*, "GREIT: A unified approach to 2D linear EIT reconstruction of lung images," *Physiol. Meas.*, vol. 30, no. 6, pp. S35–S55, 2009.

[60] S. Russo, S. Nefti-Meziani, N. Carbonaro, and A. Tognetti, "A quantitative evaluation of drive pattern selection for optimizing EIT-based stretchable sensors," *Sensors*, vol. 17, no. 9, p. 1999, 2017.

[61] W. R. B. Lionheart, "EIT reconstruction algorithms: Pitfalls, challenges and recent developments," *Physiol. Meas.*, vol. 25, no. 1, pp. 125–142, 2004.

[62] H. Gagnon, M. Cousineau, A. Adler, and A. E. Hartinger, "A resistive mesh phantom for assessing the performance of EIT systems," *IEEE Trans. Biomed. Eng.*, vol. 57, no. 9, pp. 2257–2266, Sep. 2010.

[63] B. Sun, S. Yue, Z. Cui, and H. Wang, "A new linear back projection algorithm to electrical tomography based on measuring data decomposition," *Meas. Sci. Technol.*, vol. 26, no. 12, 2015, Art. no. 125402.

[64] B. Grychtol, W. R. B. Lionheart, M. Bodenstein, G. K. Wolf, and A. Adler, "Impact of model shape mismatch on reconstruction quality in electrical impedance tomography," *IEEE Trans. Med. Imag.*, vol. 31, no. 9, pp. 1754–1760, Sep. 2012.

[65] S. de Gelidi *et al.*, "Torso shape detection to improve lung monitoring," *Physiol. Meas.*, vol. 39, no. 7, 2018, Art. no. 074001.

[66] S. de Gelidi *et al.*, "Thoracic shape changes in newborns due to their position," *Sci. Rep.*, vol. 11, no. 1, p. 4446, 2021.

[67] M. Takhti and K. Odame, "Structured design methodology to achieve a high SNR electrical impedance tomography," *IEEE Trans. Biomed. Circuits Syst.*, vol. 13, no. 2, pp. 364–375, Apr. 2019.

[68] B. Liu *et al.*, "A 13-channel 1.53-mW 11.28-mm^2 electrical impedance tomography SoC based on frequency division multiplexing for lung physiological imaging," *IEEE Trans. Biomed. Circuits Syst.*, vol. 13, no. 5, pp. 938–949, Oct. 2019.

[69] L. Yan *et al.*, "A 13 μA analog signal processing IC for accurate recognition of multiple intra-cardiac signals," *IEEE Trans. Biomed. Circuits Syst.*, vol. 7, no. 6, pp. 785–795, Dec. 2013.

[70] N. Van Helleputte *et al.*, "A 345 μW multi-sensor biomedical SoC with bio-impedance, 3-channel ECG, motion artifact reduction, and integrated DSP," *IEEE J. Solid-State Circuits*, vol. 50, no. 1, pp. 230–244, Jan. 2015.

[71] N. Van Helleputte, S. Kim, H. Kim, J. P. Kim, C. Van Hoof, and R. F. Yazicioglu, "A 160 μA biopotential acquisition IC with fully integrated IA and motion artifact suppression," *IEEE Trans. Biomed. Circuits Syst.*, vol. 6, no. 6, pp. 552–561, Dec. 2012.

[72] S. Subhan and S. Ha, "A harmonic error cancellation method for accurate clock-based electrochemical impedance spectroscopy," *IEEE Trans. Biomed. Circuits Syst.*, vol. 13, no. 4, pp. 710–724, Aug. 2019.

[73] W. A. Evans and M. S. Towers, "Hybrid technique in waveform generation and synthesis," *IEE Proc. G Electron. Circuits Syst.*, vol. 127, no. 3, pp. 119–128, 1980.

[74] M. Zamani, Y. Rezaeiyan, O. Shoaei, and W. A. Serdijn, "A 1.55 μW bio-Impedance measurement system for implantable cardiac pacemakers in 0.18 μm CMOS," *IEEE Trans. Biomed. Circuits Syst.*, vol. 12, no. 1, pp. 211–221, Feb. 2018.

[75] Y. Wu, D. Jiang, M. Habibollahi, N. Almarri, and A. Demosthenous, "Time stamp—A novel time-to-digital demodulation method for bioimpedance implant applications," *IEEE Trans. Biomed. Circuits Syst.*, vol. 14, no. 5, pp. 997–1007, Oct. 2020.

[76] Y. Wu, D. Jiang, P. Langlois, R. Bayford, and A. Demosthenous, "A CMOS current driver with built-in common-mode signal reduction capability for EIT," in *Proc. 43rd IEEE Eur. Solid-State Circuits Conf. (ESSCIRC)*, Leuven, Belgium, 2017, pp. 227–230.

[77] J. Xu *et al.*, "A 665 μW silicon photomultiplier-based NIRS/EEG/EIT monitoring ASIC for wearable functional brain imaging," *IEEE Trans. Biomed. Circuits Syst.*, vol. 12, no. 6, pp. 1267–1277, Dec. 2018.

[78] L. Constantinou, I. F. Triantis, R. Bayford, and A. Demosthenous, "High-power CMOS current driver with accurate transconductance for electrical impedance tomography," *IEEE Trans. Biomed. Circuits Syst.*, vol. 8, no. 4, pp. 575–583, Aug. 2014.

[79] N. Neshatvar, P. Langlois, R. Bayford, and A. Demosthenous, "Analog integrated current drivers for bioimpedance applications: A review," *Sensors (Basel)*, vol. 19, no. 4, p. 756, 2019.

[80] P. J. Langlois, Y. Wu, R. H. Bayford, and A. Demosthenous, "On the application of frequency selective common mode feedback for multifrequency EIT," *Physiol. Meas.*, vol. 36, no. 6, pp. 1337–1350, 2015.

[81] P. O. Gaggero, A. Adler, J. Brunner, and P. Seitz, "Electrical impedance tomography system based on active electrodes," *Physiol. Meas.*, vol. 33, no. 5, pp. 831–847, 2012.

[82] H. Alzaher and M. Ismail, "A CMOS fully balanced differential difference amplifier and its applications," *IEEE Trans. Circuits Syst. II, Analog Digit. Signal Process.*, vol. 48, no. 6, pp. 614–620, Jun. 2001.

[83] Y. Wu, D. Jiang, A. Bardill, S. De Gelidi, R. Bayford, and A. Demosthenous, "A high frame rate wearable EIT system using active electrode ASICs for lung respiration and heart rate monitoring," *IEEE Trans. Circuits Syst. I, Reg. Papers*, vol. 65, no. 11, pp. 3810–3820, Nov. 2018.

[84] A. Worapishet, A. Demosthenous, and X. Liu, "A CMOS instrumentation amplifier with 90-dB CMRR at 2-MHz using capacitive neutralization: Analysis, design considerations, and implementation," *IEEE Trans. Circuits Syst. I, Reg. Papers*, vol. 58, no. 4, pp. 699–710, Apr. 2011.

[85] A. Worapishet and A. Demosthenous, "Generalized analysis of random common-mode rejection performance of CMOS current feedback instrumentation amplifiers," *IEEE Trans. Circuits Syst. I, Reg. Papers*, vol. 62, no. 9, pp. 2137–2146, Sep. 2015.

[86] H. Ha, C. Van Hoof, and N. Van Helleputte, "Measurement and analysis of input-signal dependent flicker noise modulation in chopper stabilized instrumentation amplifier," *IEEE Solid-State Circuits Lett.*, vol. 1, no. 4, pp. 90–93, Apr. 2018.

[87] S. Hong, J. Lee, J. Bae, and H.-J. Yoo, "A 10.4 mW electrical impedance tomography SoC for portable real-time lung ventilation monitoring system," *IEEE J. Solid-State Circuits*, vol. 50, no. 11, pp. 2501–2512, Nov. 2015.

[88] R. Martins, S. Selberherr, and F. A. Vaz, "A CMOS IC for portable EEG acquisition systems," *IEEE Trans. Instrum. Meas.*, vol. 47, no. 5, pp. 1191–1196, Oct. 1998.

[89] H. Chandrakumar and D. Marković, "A high dynamic-range neural recording chopper amplifier for simultaneous neural recording and stimulation," *IEEE J. Solid-State Circuits*, vol. 52, no. 3, pp. 645–656, Mar. 2017.

[90] A. J. Rao, E. K. Murphy, M. Shahghasemi, and K. M. Odame, "Current-conveyor-based wide-band current driver for electrical impedance tomography," *Physiol. Meas.*, vol. 40, no. 3, 2019, Art. no. 034005.

[91] N. Neshatvar, P. Langlois, and A. Demosthenous, "A non-linear feedback current driver with automatic phase compensation for bioimpedance applications," *IEEE Trans. Circuits Syst. II, Exp. Briefs*, vol. 65, no. 10, pp. 1340–1344, Oct. 2018.

[92] Y. Yang and J. Jia, "A multi-frequency electrical impedance tomography system for real-time 2D and 3D imaging," *Rev. Sci. Instrum.*, vol. 88, no. 8, 2017, Art. no. 085110.

[93] C. Tan, S. Liu, J. Jia, and F. Dong, "A wideband electrical impedance tomography system based on sensitive bioimpedance spectrum bandwidth," *IEEE Trans. Instrum. Meas.*, vol. 69, no. 1, pp. 144–154, Jan. 2020.

[94] Z. Zhao, F. Fu, and I. Frerichs, "Thoracic electrical impedance tomography in Chinese hospitals: A review of clinical research and daily applications," *Physiol. Meas.*, vol. 41, no. 4, 2020, Art. no. 04TR01.

[95] Y. Wu, D. Jiang, N. Neshatvar, F. Fahimi. Hanzaee, and A. Demosthenous, "Towards a universal methodology for performance evaluation of electrical impedance tomography systems using full reference SNR," in *Proc. IEEE Int. Symp. Circuits Syst. (ISCAS)*, Seville, Spain, 2020, pp. 1–5.
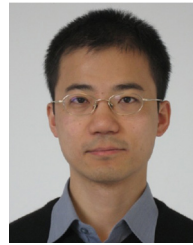
DAI JIANG (Senior Member, IEEE) received the B.Sc. and M.Sc. degrees from the Beijing University of Aeronautics and Astronautics, China, in 1998 and 2001, respectively, and the Ph.D. degree from University College London (UCL), U.K., in 2009.

His Ph.D. work was on frequency synthesis. He was with Datang Telecom Group, China, from 2001 to 2002, working on developing FPGA functions for WCDMA signal processing. From 2006 to 2020, he was a Research Fellow with the Bioelectronics Group, UCL, where he is currently a Lecturer with the Department of Electronic and Electrical Engineering. His research interests include CMOS analog and mixed-signal integrated circuit design for biomedical applications. He is a member of the Biomedical and Life Science Circuits and Systems Technical Committee of the IEEE Circuits and Systems Society.

RICHARD H. BAYFORD (Life Senior Member, IEEE) received the M.Sc. degree in industrial systems from Cranfield University, Cranfield, U.K., and the Ph.D. degree from Middlesex University, London, U.K., in 1994.

He was appointed a Professor of Bio-Modeling and Informatics with the Department of Natural Sciences, Middlesex University, U.K., in 2005, and he is a Visiting Professor with the Department of Electrical and Electronic Engineering, University College London, London, U.K. He has authored more than 300 papers in journals and international conference proceedings. His expertise is in biomedical image/signal processing, electrical impedance tomography, deep brain stimulation, bio-modeling, tele-medical systems, and VLSI design. He was the Editor-in-Chief of Physiological Measurement, Institute of Physics, from 2008 to 2013. He is on the editorial board of the *International Journal of Biomedical Imaging*. He is a Fellow of the Institute of Physics.

YU WU (Member, IEEE) received the B.Eng. degree in electronic and electrical engineering from University College London (UCL), U.K., in 2012, the M.Sc. degree in analog and digital integrated circuit design from Imperial College London, U.K., in 2013, and the Ph.D. degree in electronic and electrical engineering from UCL in 2019. From 2016 to 2018, he was a Research Associate with the Bioelectronics Group, UCL, where he has been a Research Fellow since 2019. His current research interests include human-machine interactive systems, CMOS integrated circuit design, and novel mixed-signal microelectronic systems for biomedical applications.

FARNAZ FAHIMI HANZAEE (Student Member, IEEE) received the B.Sc. degree in electronic engineering from the Iran University of Science and Technology, Iran, in 2014, the M.Sc. degree in bioengineering from the Amirkabir University of Technology (Tehran Polytechnic), Iran, in 2018, and the M.Res. degree in neurotechnology from Imperial College London, U.K., in 2019. She is currently pursuing the Ph.D. degree in electronic and electrical engineering with the Bioelectronics Group, University College London. She is currently a Research Assistant. Her research interests include CMOS analog and mixed-signal circuit design and organic electronics for biomedical applications.

ANDREAS DEMOSTHENOUS (Fellow, IEEE) received the B.Eng. degree in electrical and electronic engineering from the University of Leicester, Leicester, U.K., in 1992, the M.Sc. degree in telecommunications technology from Aston University, Birmingham, U.K., in 1994, and the Ph.D. degree in electronic and electrical engineering from University College London (UCL), London, U.K., in 1998.

He is a Professor with the Department of Electronic and Electrical Engineering, UCL, and leads the Bioelectronics Group. He has made outstanding contributions to improving safety and performance in integrated circuit design for active medical devices, such as spinal cord and brain stimulators. He has authored more than 300 articles in journals and international conference proceedings, several book chapters, and holds several patents. His research interests include analog and mixed-signal integrated circuits for biomedical, sensor, and signal processing applications. He was a co-recipient of a number of best paper awards and has graduated many Ph.D. students. He was an Associate Editor from 2006 to 2007, the Deputy Editor-in-Chief of the IEEE TRANSACTIONS ON CIRCUITS AND SYSTEMS—II: EXPRESS BRIEFS from 2014 to 2015, an Associate Editor from 2008 to 2009, and the Editor-in-Chief of the IEEE Transactions on Circuits and Systems—I: Regular Papers from 2016 to 2019. He is an Associate Editor of the IEEE TRANSACTIONS ON BIOMEDICAL CIRCUITS AND SYSTEMS and serves on the International Advisory Board of Physiological Measurement. He has served on the technical committees for a number of international conferences, including the European Solid-State Circuits Conference, the International Symposium on Circuits and Systems, and the International Conference on Electronics, Circuits, and Systems. He is a Fellow of the Institution of Engineering and Technology and a Chartered Engineer.